*Journal of The Electrochemical Society*, 2021 **168** 024511

# Transformation of the OER-Active $IrO_x$ Species under Transient Operation Conditions in PEM Water Electrolysis

**Philipp Jan Rheinländer**[a,*,z] **and Julien Durst**

*Chair of Technical Electrochemistry, Department of Chemistry and Catalysis Research Center, Technische Universität München, 85748 Garching, Germany*

Iridium oxides are common oxygen evolution catalysts, combining high activity with decent stability. However, these properties vary strongly with the $IrO_x$ form, ranging from durable crystalline $IrO_2$ to more active but less stable amorphous, hydrous oxides. Herein we demonstrate how an operation transient during proton exchange membrane water electrolysis (PEMWE) can induce conversion of $IrO_2$ in the anode catalyst layer into a more hydrous form. We operate a 5 $cm^2$ PEMWE cell at 80 °C and elevated $H_2$ pressure, then interrupt the power supply and observe the OCV showing a characteristic decay to eventually 0 V. We postulate that the $IrO_2$ surface reacts with $H_2$ crossing over the membrane, confirm ex situ via TGA and XRD analyses that $IrO_x$ can be reduced to metallic Ir under $H_2$ at 80 °C, elaborate the related thermodynamics and match them with the electrochemical potential of the $IrO_x$ catalyst during the above transient. This is supported in situ via cyclic voltammograms and polarization curves showing improved OER activity. Moreover, we demonstrate that subsequent polarization to the OER potential range transforms the reduced catalyst surface into a more hydrous $IrO_x$ and wrap up with implications for the long-term performance and durability of PEMWE devices.

 [DOI: 10.1149/1945-7111/abe0d4]

Manuscript submitted August 13, 2020; revised manuscript received January 24, 2021. Published February 10, 2021. *This paper is part of the JES Focus Issue on Proton Exchange Membrane Fuel Cell and Proton Exchange Membrane Water Electrolyzer Durability. This was Paper 2427 presented at the Honolulu, Hawaii, Meeting of the Society, October 2–7, 2016.*

Renewable $H_2$ production is a prerequisite for successfully establishing fuel cell-based electromobility and hydrogen infrastructure. In this respect, proton exchange membrane water electrolysis (PEMWE) has attracted strong interest, not least due to the high efficiency and enormous power densities possible in these devices.[1] Research is mainly focused on the anode side, where the oxygen evolution reaction (OER) takes place, causing the vast majority of kinetic losses.[2] In the acidic environment of a PEM and at the anode's harsh potentials of >1.4 $V_{RHE}$, OER catalysts of choice are usually iridium oxide ($IrO_x$) based owing to their decent activity and acceptable stability.[3–6] In order to provide the basis for the discussion of the phenomena observed in this study, we first give an introduction into dry and hydrous iridium oxides, describe the physical and electrochemical properties and their formation and transformation, and finally discuss the chemical reduction of $IrO_x$ under $H_2$ and work out the related thermodynamics. Note that this introduction is referring only to acidic electrolytes. In alkaline, $IrO_x$ are usually not considered for OER catalysis, due to their higher corrosion rates, and because they can easily be replaced by inexpensive, non-noble metal–based catalysts without activity penalties.[5,7–10]

Throughout the past five decades, iridium oxides have been the scope of countless studies investigating not only their OER electrochemistry, but even more excessively their different forms, which range from "dry" to "hydrous" Ir oxides.[11] While the former term is commonly used for a crystalline (rutile structure), compact, highly conductive, stoichiometric $IrO_2$,[12–14] hydrous oxides are amorphous, porous and permeable for water and protons, and their electronic conductivity varies with the electrochemical potential, which leads to distinct electrochromic properties.[15] Their structure was described as an open, "gel-like" 3D network of oxo-bridged $IrO_xH_y$ complexes[16] with a ~6-times lower effective (i.e. dry) density as compared to crystalline $IrO_2$, equivalent to a >80 % pore volume fraction available for percolation with electrolyte.[17] The according increase in effective electrode-electrolyte interface makes a large fraction of the Ir ions accessible for electrochemical oxidation and reduction, leading to an enormous electrochemical pseudocapacity per electrode area which marks also the outstanding eligibility of hydrous Ir oxides for supercapacitor materials.[18] In the potential window between the onsets of HER and OER, and in acidic electrolyte, the relevant oxidation state transfer is the transition between Ir(III) and Ir(IV) oxides around 0.9 $V_{RHE}$, which is highly reversible in consecutive anodic and cathodic potential scans.[17,19–21] Thereby, an "injection-ejection" mechanism of electrolyte species through the electrode's pores was postulated to compensate the capacitive currents drawn from the electrode during voltammetry. For aqueous, acidic electrolytes, this was reported to be carried out exclusively by protons and water, depending on the material's hydration degree which can vary with the distance from the electrode surface.[17,22] In contrast, for $IrO_2$ single crystal surfaces, the proton penetration depth was found to be limited to the topmost 1–2 monolayers (ML).[14] Analyses by Gottesfeld et al. revealed that hydrous $IrO_x$ films of several 100's nm thickness, contributed with 0.5–1 electrons per Ir atom in the layer to the capacitive charge measured via cyclic voltammetry in 0.5 M sulphuric acid and below the OER onset potential at ~1.4 $V_{RHE}$.[23] This is indicative not only of a relatively high electronic and ionic accessibility of the oxide layer despite its remarkable thickness, but also of the presence of Ir (III) species above 1.4 $V_{RHE}$. Based on optical in situ measurements in the same study, they ascribed a semiconducting nature to these films in the OER potential region and deduced that the coexistence of Ir(III) and Ir(IV) species entails a "mixed-valence defect structure" with better electronic conductivity and more active sites. Recent studies using X-ray Absorption Spectroscopy (XAS) verified the presence of Ir(III) and also that of Ir(V) during OER on hydrous $IrO_x$[24] and, moreover, found short-range crystalline domains similar to that of rutile-type $IrO_2$, which are maintained during oxygen evolution.[25,26]

In the context of OER catalysis, the different physical properties of these Ir oxides affect significantly their activity, whereby the hydrous form is clearly superior, as expressed in both, lower overpotentials and lower Tafel slopes.[23,27–31] The former is usually justified with the porous structure described above, which can be seen quasi as an extension of the $IrO_x$' dispersion,[20,32–34] and was put in a nutshell by Burke and O'Sullivan calling hydrous Ir oxides a "three-dimensional electrocatalyst for the OER."[35] On the other hand, the OER on crystalline $IrO_2$ is limited to the Ir sites at their

*Electrochemical Society Member.
[a]Present address: FTXT Energy Technology Co., Ltd, Great Wall Motor Holdings, Baoding, Hebei, 071000, People's Republic of China.
[z]E-mail: rheinlaender@tum.de

surface. The lower Tafel slope obtained with hydrous $IrO_x$ was discussed as indicator for a change in reaction mechanism, resulting from an altered electrophilicity of the Ir sites.[23]

Gottesfeld and Srinivasan stated already in the late 1970's: "the formation of the '*right type of oxide*' may indeed improve the catalytic activity on noble-metal oxygen electrodes".[23] Furthermore, they already brought into play that their resistance towards dissolution developed oppositely to the trend in activity, by mentioning a "possible *trade-off* between activity and stability." The ongoing quest for this *right type of oxide* has led to a surge of publications in the field dealing with preparation and modification of Ir oxides as well as their structural and electrochemical characterization, and has confirmed all in all that OER activity and stability evolve contrarily. Thereby, a lack of "stability" is usually considered to appear in the form of dissolution (proven during high anodic potentials[7,23,36] and potential transients[30]), or as deactivation of active sites.[23,37] The latter was explained by a decrease in electrophilicity of Ir sites through deprotonation of hydrous oxides at high potentials (this was demonstrated to re-activate when polarized to low potentials), and also by a loss of ECSA due to irreversible restructuring of the electrode-electrolyte interface. Hence, there is strong experimental indication that the reasons for high activity and low stability of hydrous oxides originate from the same physical properties, in particular their amorphous structure, porosity, reduced electronic conductivity, fast (de)protonation, highly reversible redox behavior and the presence of Ir(III) sites up to the OER potential regime. Consequently, it appears unlikely that the *right type* of $IrO_x$ exists in one universal form, but rather has to be specially designed depending on the terms of application. This is even more challenging with regard to the question if these tailored properties can then at all be retained under the conditions of an operating electrolyzer anode, which will be discussed below in more detail. Moreover, some authors even go as far as to postulate an intrinsic connection between the evolution of oxygen and the dissolution of the catalyst: Markovic and coworkers claimed from studies of various noble metal surfaces a "functional link between activity and stability of monometallic oxides during the OER in acidic media"[38] and even stated that "if the oxide is stable then it is completely inactive for the OER."[39] Recently, Geiger and Kasian et al. introduced a universal method to quantify the correlation between activity and stability of electrocatalysts: The so-called *stability number* is defined as the ratio between reaction turnover and dissolution rate, i.e., in case of OER on Ir oxides, the number of evolved $O_2$ molecules divided by the number of Ir atoms dissolved thereby.[40] Thus, the stability number can be used as a metric for the "productivity" over the "deterioration" of an electrocatalyst. Experiments with different $IrO_x$ samples in aqueous electrolyte yielded 1−2 orders of magnitude higher stability numbers for a crystalline $IrO_2$ compared to a hydrous $IrO_x$ (measured in an on-line SFC setup, see below paragraph). This indicates a significantly higher OER lifetime productivity of thermal $IrO_2$ and also confirms the hypothesis that OER is always accompanied by a certain dissolution of the $IrO_x$ catalyst. Another metric for basically the same relation was suggested as *activity-stability factor* by Kim et al. and published quasi at the same time.[41] Thermodynamic considerations came to the point that metal oxides are basically unstable above the reversible oxygen potential and concluded that reconciliation of activity with stability can only be achieved by a metastable oxide where the mobility of oxide ions is fully suppressed in the bulk of the material.[42] In this respect, besides tuning the morphology and hydration degree of Ir oxides, there are alternative strategies to enhance their activity and stability, e.g. by alloying or mixing with $RuO_2$,[43–45] or by adding oxides of non-noble metals such as Ti, Sn or Ta. A detailed review of binary and ternary oxides as OER catalysts is given e.g. in Ref. 5

A general problem evolves from how activity and stability are analyzed: While activity is usually measured directly via potentiodynamic or chrono methods, electrochemical stability is commonly assessed indirectly via the evolution or degradation of the OER activity under an ageing protocol, or via post mortem analyses. Within the past few years, Cherevko, Mayrhofer and coworkers enriched the research community introducing an on-line technique allowing for the direct quantification of dissolution products emitted from an electrode that is subjected to a specific current/potential profile.[46] This method has been established using a so-called scanning flow cell (SFC) with a downstream time-resolved analysis via inductively coupled plasma mass spectrometry (ICP-MS), which, however, requires the usage of liquid electrolytes. Activity trends assessed in half cell tests with liquid electrolytes commonly hold true in polymer electrolyte full cells, as has been generally confirmed for Ir oxides during the past decade.[47,48] On the other hand, this analogy does not necessarily apply to catalyst durability, which can change completely considering different ion transport mechanisms, concentration profiles and the absence of convection in solid electrolytes. Studies of $IrO_x$ stability in full cells are quite rare, often limited to very short ageing periods, and mostly confined to the measurement of overall performance degradation during constant operation or under an artificial load profile.[49–52] Thus, to allow for conclusions on the catalyst stability, the losses would need to be properly disentangled from other degradation processes such as corrosion of porous transport layers (PTL) and flow fields, or ionomer poisoning by feed water impurities or cathodic dissolution products. In an attempt to deliver a quantitative estimate of how different the stability of OER catalysts is in liquid vs polymer electrolyte, Geiger et al. estimated the stability number of $RuO_2$ in a PEMWE from a data set available in the literature. The value was found 2−3 orders of magnitude higher than that measured with the same $RuO_2$ in aqueous electrolyte (see Ref. 40 SI), which emphasizes that durability data from half-cell measurements is not directly applicable to full cells.

Furthermore, it shall be mentioned at this point that a recurrent shortcoming in durability considerations is that in a PEMWE cell, the potential relevant for the (in)stability of the anode catalyst cannot be equalized with the cell voltage including all loss terms. Instead, it is determined only by the surface potential of the active material, i.e., the sum of the reversible potential ($E_{rev}$) and the kinetic overpotential under the given conditions. Thorough full cell analyses from our lab have shown recently that this surface potential is reasonably low for a state of the art $IrO_2$ based catalyst and realistic conditions (~1.5 $V_{RHE}$ at 1 $Acm^{-2}$, 80 °C and ~2 $mg_{Ir}$ $cm^{-2}$), and can be expected to not exceed 1.6 V even at a tenfold lower Ir-loading and tenfold higher current density, considering the reported Tafel slope of 46 mV $dec^{-1}$.[2]

Iridium oxides are commonly prepared as nanoparticles (NP) for electrocatalysis, or as films, e.g. for electrochromic application. Iridium oxide NPs can be synthesized from suitable precursors through e.g. Adams fusion, sol-gel or colloidal methods.[47,49,53–57] Synthesis of $IrO_x$ films ("IROFs") was accomplished through thermal decomposition of Ir precursors like $IrCl_3$,[58] via electrodeposition from precursor solutions ("EIROFs"),[26,59] sputtering ("SIROFs")[60,61] or by anodic oxidation of iridium surfaces ("AIROFs").

The latter were object of the vast majority of fundamental $IrO_x$ studies, grown electrochemically via potential cycling of Ir electrodes in aqueous electrolytes. This was probably initially reported in 1961 by Böld and Breiter,[62] while the detailed investigation and respective nomenclature followed over one decade later, classifying them as hydrous $IrO_x$ films ("HIROFs").[36,63–65] Burke and O'Sullivan proposed the presence of a "duplex oxide film" featuring an ultrathin (1–5 Mls) compact, and largely anhydrous oxide skin at the interface between Ir bulk and hydrous $IrO_x$ layer,[35] analogously to a model developed earlier for $Au/AuO_x$ interfaces.[66] This skin was found later to be the actual breeding ground for the hydrous oxide through its consecutive reduction and re-oxidation under potential cycling:[30,67,68] It forms through oxidation of the Ir bulk surface in an anodic potential sweep, which is then reduced back only incompletely in the subsequent cathodic scan,[20] whereby its outer fraction is transformed into hydrous $IrO_x$ and added to the HIROF (one ML per cycle, according to Ref. 68). Hence, maximum lower and minimum upper potential boundaries have to be complied

with in the cycling procedure to allow for these transitions in the compact oxide skin,[7,19,23,62,64] which explains also why hydrous oxides cannot be obtained through potentiostatic treatment of Ir surfaces.[7,19,69] These "critical limits" are situated around 0.2 $V_{RHE}$ and 1.4 $V_{RHE}$ ($E_{lower}$ and $E_{upper}$, respectively), and vary slightly with the electrolyte type and concentration, as well as with the applied scan rate and potential profile.[68] Furthermore, HIROF growth is faster under square wave potential cycling as compared to triangular waves,[27] which Pickup and Birss founded by a detailed growth mechanism.[68] HIROFs were reported to reach several 100 s of nm in thickness,[23] probably only limited by eventual physical detachment from the electrode.[35] The key to this irreversible transformation of Ir into hydrous $IrO_x$ was explained as follows: In the cathodic scan, the HIROF is reduced together with the vicinal fraction of the "dry" interlayer, to form hydrous Ir(III) oxide around 0.9 $V_{RHE}$, which, however, does not undergo any further reduction at more cathodic potentials (not even below 0 $V_{RHE}$).[64] This is most probably due to their negligible electric conductivity,[22,23] leading to "switched off" $IrO_x$ according to Conway and Mozota,[20] i.e., the so-called bleaching of hydrous $IrO_x$ during cathodic potential scans, responsible for their electrochromic properties.[15,20] On the other side, the $IrO_x$ adjacent to the Ir substrate gets reduced back to metallic Ir at a sufficiently low potential, where it is available for hydrogen underpotential deposition (H-UPD), almost like a HIROF-free iridium electrode.[64]

According to studies by Cherevko et al. in a scanning flow cell (SFC), potential cycling of a HIROF-covered Ir electrode is accompanied by significant dissolution, which strongly depends on the cycled potential window: While cathodic dissolution reaches a maximum with $E_{upper} \approx 1.4$ $V_{RHE}$, anodic dissolution evolves exponentially with the increase of this value and exceeds the cathodic dissolution at $E_{upper} > 1.5$ $V_{RHE}$.[30] The latter is in agreement with early findings that HIROFs dissolve anodically when polarized to >1.6 $V_{RHE}$.[7,23,36] Interestingly, strong cathodic dissolution requires an $E_{lower}$ of <0.2 $V_{RHE}$, i.e., coherent with the critical potential limits for the electrochemical growth of HIROFs, as stated above. Moreover, analyses of a metallic Ir electrode show that their dissolution under *E*-cycling is somewhat lower than the one covered with HIROF, but has about the same dependence on the potential boundaries.[30,70] It appears therefore likely that the cathodic dissolution of Ir originates mainly from the reduction of the compact $IrO_x$ skin covering the Ir bulk, complemented by corrosion of the grown hydrous $IrO_x$ layer, which hardly depends on the potential sweep direction and boundaries. Consequently, the growth of HIROFs on a metallic Ir substrate seems to be intrinsically tied together with dissolution.

Hydrous $IrO_x$ is being transformed into dry $IrO_x$ upon heat treatment in inert or oxidizing atmosphere, whereby their structure and with it their OER activity and corrosion resistance can be tailored via the calcination temperature.[27–29,31,46,58,71] The transition was located in a broad range around 200 °C–400 °C,[29,31,46] whereby the form of $IrO_x$ depends already strongly on the temperature of their synthesis route and can be further modified by subsequent heat treatment.[47–49,56,57] Hence, dry and crystalline $IrO_2$ is obtained as thermal oxide, either by calcination of a hydrous oxide or directly in a synthesis at temperatures above 400 °C. Note that in the relevant temperature range, calcination of nanostructured $IrO_x$ involves already a remarkable sintering especially of unsupported $IrO_x$ particles, diminishing the powder's dispersion degree (e.g. for a highly dispersed $IrO_x$ powder synthesized via polyol method at 160 °C, a 10-fold increase of average particle size was reported after 1 h tempering at 500 °C in air).[56] Therefore, studying the effect of calcination temperature on activity and stability of $IrO_x$ NPs is more complex than when films are investigated.

Interestingly, in the opposite direction, crystalline $IrO_2$ can be transformed into hydrous $IrO_x$ by excessive potential cycling in a potential range similar to that inducing the growth of HIROF on Ir (i.e., ~0–1.5 $V_{RHE}$), which was proposed to be harsh enough to distort the $IrO_2$ crystal structure at its surface.[14,28] This finding shows that the anticipated activity and stability of an $IrO_x$ with tailored properties is not only a matter of how the sample was initially customized, but depends also on the respective operation conditions. To be specific, the choice of thermal $IrO_x$ which due to durability constraints is the preferred form for most applications as OER catalyst, does not necessarily grant an extended lifetime, unless repetitive potential transients can be inhibited during operation. Furthermore, a recent study by Strasser and coworkers analyzed how Ir oxides can be reduced under hydrogen, whereby their structure plays an important role: Silicon supported HIROFs calcined at temperatures between 250 °C and 550 °C were subjected to temperature programmed reduction (TPR) in dilute $H_2$, which took place at ~70 °C for the amorphous samples, while the most crystalline film reacted only at ~180 °C.[29] Since metallic Ir is more prone to dissolution during OER,[46,70] their results raise further concerns about the stability of $IrO_x$ in electrochemical devices. Moreover, they open another potential path to convert crystalline into amorphous Ir oxide, considering the well-known growth of hydrous $IrO_x$ on metallic Ir. In fact, the reduction of IROFs under hydrogen or argon (chemical reduction and thermal decomposition, respectively) has already been studied decades ago, however, not with regard to their application in electrocatalysis.[72,73] In accordance with Ref. 29 the respective reaction temperatures were found to rise with increasing crystallinity of the IROFs. The consequent questions of interest for oxygen evolving anodes are these: In how far can $IrO_x$ catalysts come into contact with $H_2$ during their application, and under which conditions will their reduction take place?

Due to their superior OER activity compared to Pt, iridium oxides are as well utilized as co-catalysts in fuel cell anodes to mitigate anode carbon corrosion during cell reversal events triggered by global fuel starvation.[74–76] Thereby, the anode side of one cell in a fuel cell stack is not sufficiently supplied with $H_2$, e.g. due to non-unique pressure drops between the cells, or the lack of system fuel supply control during steep power transients.[74,76] In case the stack is under sufficient load, the concerned anode will no longer be able to provide the stack current from the oxidation of $H_2$, and instead start to oxidize water (OER) and the carbon support (carbon oxidation reaction, COR) in the catalyst layer.[77] Since the latter can destroy the anode within seconds, one major strategy to mitigate the damage from cell reversal is to kinetically enhance the OER by the addition of an OER-active co-catalyst to the anode catalyst layer. Cell reversal tests (CRT) at 80 °C have shown that only 1 $\mu g_{Ir} cm^{-2}$ added in the form of $IrO_x$ to a conventional anode comprising Vulcan carbon supported platinum, could enhance the contribution of OER to the total current from <5 % to >95 % at a CRT current of 200 mA $cm^{-2}$.[78]

However, recent studies in our labs raised doubts that the effectiveness of such cell reversal-tolerant anodes can be maintained over an extended range of fuel cell operation. Even though the performed experiments were start-up/shut-down (SUSD), i.e., common cathode degradation tests, they harmed also the anodes' CRT tolerance indicating a partial loss of the OER active species. Since the utilized co-catalyst was a thermal $IrO_x$ (with $x \approx 2$) which is relatively stable towards dissolution,[27,31,46,58] we suspected that its crystallinity and oxidation state could not be conserved in the environment of an operating PEMFC anode. These conditions are usually: temperature of 60 °C–100 °C, $H_2$-rich atmosphere at a $H_2$ pressure of 100–300 kPa, relative humidification around 50%–100%, and a respective electrochemical potential between 0 and <10 $mV_{RHE}$,[79,80] depending on the Pt loading and the drawn HOR current. Considering the fact that platinum group metals (PGM) like Pt, Pd, and Ir start to form surface oxides only at much higher potentials, as evident from cyclic voltammograms (CV),[81] it appears rather unlikely that $IrO_x$ is stable over an extended period of time in a PEMFC anode. The same conclusion must be drawn from the respective Pourbaix diagram, where the only stable phase under these conditions should be metallic Ir.[21]

According to thermodynamic data available in the literature, the chemical reduction of $IrO_2$ to metallic Ir under $H_2$ (Eq. 1) is highly

exergonic. Based on the values reported in Refs. 12, 82, the respective standard Gibb's free energy of reaction ($\Delta_rG^\circ$) is $-256.7$ kJmol$^{-1}$ at 25 °C (298 K), 101.3 kPa $H_2$ pressure, and for the formation of liquid water (see Table I for details).

$$IrO_2 + 2H_2 \rightarrow Ir + 2H_2O \quad \Delta rG^\circ = -256.7\ \text{kJmol}^{-1} \qquad [1]$$

Rewriting Eq. 1 as electrochemical reaction, it splits up into Eqs. 2 and 3 (reduction and oxidation, in the respectively depicted directions), of which the latter is the well-known hydrogen oxidation (and evolution) reaction (HOR/HER).

$$IrO_2 + 4H^+ + 4e^- \rightarrow Ir + 2H_2O \qquad [2]$$

$$2H_2 \rightarrow 4H^+ + 4e^- \qquad [3]$$

Their individual $\Delta_rG^\circ$ values can be translated into respective reversible electrochemical potentials ($E_{rev}$) via Eq. 4.

$$E_{rev} = \frac{-\Delta_rG^\circ}{n \cdot F} \qquad [4]$$

Where $n$ is the number of electrons transferred in one reaction sequence (i.e. 4 in case of Eq. 2), and $F$ is the Faraday constant. Considering that $E_{rev}$ of Eq. 3 is by definition 0 V on the reversible hydrogen electrode (RHE) scale, the reversible potential of the electrochemical reduction of $IrO_2$ (Eq. 2) can be calculated for the RHE scale using the $\Delta_rG^\circ$ value from Eq. 1, which yields 665 $mV_{RHE}$ for the formation of liquid water. For temperatures other than 25 °C, the deviation of $\Delta_rG$ from the standard value can be estimated taking into account the changes of standard entropy and standard heat capacity over the course of the reaction ($\Delta_rS^\circ$ and $\Delta_rc_p^\circ$, respectively), following Eq. 5.[83]

$$\Delta_rG^T = \Delta_rG^\circ - \Delta_rS^\circ(T - 298\text{K}) - \Delta_rc_p^\circ\left[T \cdot \ln\left(\frac{T}{298\text{K}}\right) - (T - 298\text{K})\right] \qquad [5]$$

Where $\Delta_rG^T$ is the Gibb's free energy of reaction at a chosen temperature $T$ in Kelvin. This formula is based upon the premise that $\Delta_rc_p$ is temperature independent which we consider a reasonable assumption within the relatively narrow temperature range regarded in this study. The calculated $\Delta_rG$ of Eq. 1 for the representative operation temperature of a PEMFC MEA (i.e. 80 °C or 353 K) is summarized in Table I together with the standard values for 25 °C, accounting for both, the formation of liquid or gaseous water. The corresponding potentials were calculated using Eq. 4, and can be considered as reversible potential of the electrochemical reduction of $IrO_2$ to Ir (Eq. 2) on the RHE scale.

The numbers demonstrate that within the whole temperature range and irrespective of the aggregation state of the formed water, the regarded reduction of $IrO_2$ is clearly exergonic and thermodynamically favored at potentials below ~600 $mV_{RHE}$. Consequently, the stability of $IrO_x$ employed in a cell reversal-tolerant PEMFC anode is just a matter of the reaction kinetics of Eq. 1 at an overpotential of more than 500 mV. A more or less fast transformation to metallic Ir could be the first step initiating the observed degradation, especially with respect to its reduced stability compared to $IrO_2$ at OER potentials,[31,34,46] and under potential transients, a fortiori when low potentials close to 0 $V_{RHE}$ are involved.[34,70]

While Strasser and coworkers found via TPR experiments that their crystalline $IrO_x$ films undergo a reaction with hydrogen only at temperatures significantly above the operation range of conventional PEM devices,[29] we demonstrate in this work the reduction of a thermal $IrO_x$ catalyst under $H_2$ at only 80 °C. Furthermore, we point out how relevant this finding actually is also for the $IrO_x$ in the anode of a PEM water electrolyzer, drawing a conceivable operation scenario where it comes into contact with hydrogen, and proving our point with respective full cell tests. The consequence for the catalyst's OER activity is analyzed and possible implications to their electrochemical stability are discussed.

## Experimental

***Analytical methods.***—Thermogravimetric analysis (TGA) and differential scanning calorimetry (DSC) of $IrO_x$-based catalyst powders were performed on a *Mettler Toledo* TGS/DSC 1 STAR$^e$ instrument coupled with a *Pfeiffer Vacuum* Thermostar mass spectrometer for on line-analysis of the effluent gas. The sample was weighed into an alumina crucible closed with a perforated alumina lid and directly inserted into the TGA furnace. The latter was flushed with Ar (5.0, *Westfalen*) for 10 min at 100 ml min$^{-1}$ and 25 °C, prior to the respective heating profile with a temperature ramp of 5 K min$^{-1}$ and optionally an isothermal period at 80 °C, both in 40 ml min$^{-1}$ of 5 $\%_{vol}$ $H_2$ in Ar (5.0, *Westfalen*) with additional 20 ml min$^{-1}$ Ar as inert gas. At the end of the experiment, the gas flow was switched back to pure Ar at 100 ml min$^{-1}$ and then cooled down to 25 °C. The DSC signal was processed with a blank curve recorded with an empty crucible under otherwise equal conditions.

X-ray powder diffraction (XRD) was performed in 0.7 mm glass capillaries using a *STOE* Stadi MP diffractometer with monochromatized Mo-$k_{\alpha1}$ radiation.

Transmission electron microscopy (TEM) of catalyst powders was performed on a *JEOL* 2010 TEM at an acceleration voltage of 200 kV.

The specific surface area of catalyst powders was determined via nitrogen adsorption (Brunauer-Emmet-Teller, BET) after outgasing for 6 h at 200 °C, using a *Quantachrome* Autosorb-iQ.

***Electrolyzer cell setup.***—Membrane electrode assemblies (MEAs) with 5 cm$^2$ active area were prepared following an established decal transfer routine. Cathodes were equipped with ~0.15 $mg_{Pt}cm^{-2}$ of 46.7 $\%_{wt}$ platinum supported on Vulcan XC72 (TEC10V50E from *Tanaka*) at an ionomer-to-carbon weight ratio (I/C) of 0.7/1, while anodes comprised ~1.0 $mg_{Ir}$ cm$^{-2}$ of $IrO_x$ supported on $TiO_2$ (Elyst Ir75 0480 with 75 $\%_{wt}$ iridium from *Umicore*) and an ionomer content of 11.5 $\%_{wt}$ (i.e., I/$TiO_2$ = 1/1). The catalyst powders were dispersed with Nafion D2021 ionomer solution in 2-propanol (99.9 %) and deionized water (18 MΩcm) yielding a homogeneous ink after 18 h rolling together with 5 mm $ZrO_2$ grinding beads on a roller mixer at

**Table I. Thermodynamics of the reaction in Eq. 1: standard reaction enthalpy ($\Delta_rH^\circ$), standard reaction entropy ($\Delta_rS^\circ$), change of standard heat capacity ($\Delta_rc_p^\circ$), and Gibb's free energy ($\Delta_rG^\circ$) of the full reduction of $IrO_2$ in $H_2$ atmosphere at 25 °C and 101 kPa, forming either gaseous or liquid water. Values are calculated from the thermodynamic properties at standard conditions of the relevant reactants, given in Ref. 12, except for the $S^\circ$ values of Ir and $IrO_2$ which were taken from Ref. 82. Free energy values for 80 °C are calculated using Eq. 5, and their projection on the potential scale bases upon Eq. 4.**

| | $\Delta_rH^\circ$ [kJ mol$^{-1}$] | $\Delta_rS^\circ$ [J mol$^{-1}$ K$^{-1}$] | $\Delta_rc_p^\circ$ [Jmol$^{-1}$ K$^{-1}$] | $\Delta_rG^\circ$ [kJ mol$^{-1}$] | $\Delta_rG^\circ$ [mV] | $\Delta_rG^{80\circ C}$ [kJ mol$^{-1}$] | $\Delta_rG^{80\circ C}$ [mV] |
|---|---|---|---|---|---|---|---|
| $H_2O$ (l) | −297.56 | −136.97 | 60.73 | −256.7 | 665.2 | −249.5 | 646.5 |
| $H_2O$ (g) | −209.55 | 100.79 | −22.68 | −239.6 | 620.8 | −245.0 | 634.9 |

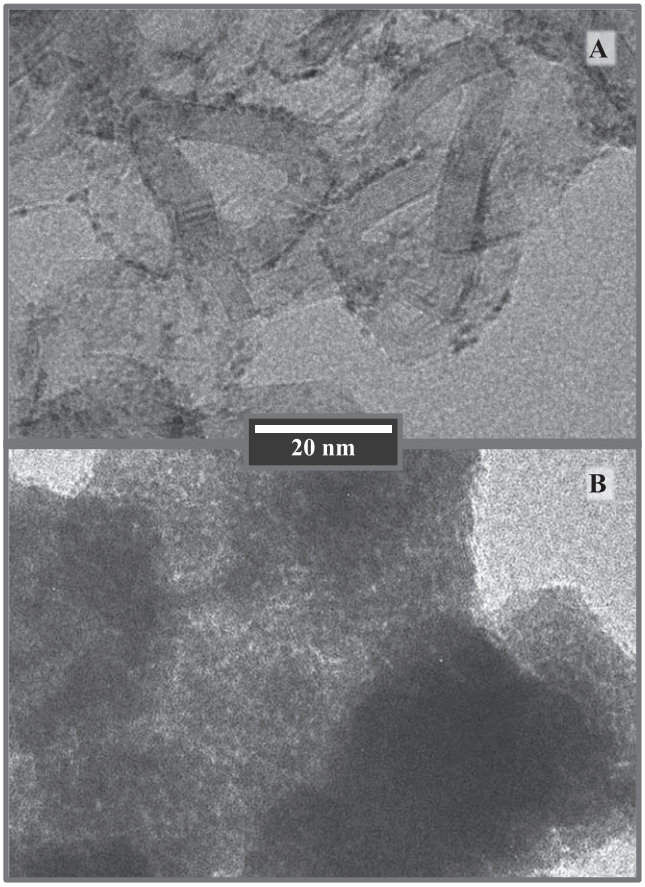


**Figure 1.** TEM micrographs of the two $IrO_x$ based catalysts investigated herein: hydrous $IrO_x$ supported on graphitized Ketjenblack (24.8 $\%_{wt}$ Ir, TKK) (A), and thermal $IrO_x$ supported on $TiO_2$ (75 $\%_{wt}$ Ir, Umicore) (B).

60 rpm. These suspensions were coated at the desired wet film thickness on a 50 $\mu$m virginal PTFE foil with a Mayer-rod coating machine and dried at 60 °C in air. Squares of 5 $cm^2$ were punched out and then laminated onto a Nafion 212 membrane (~50 $\mu$m) in a single hotpressing step using a *Dr.Collin* P200PM automatic platen press at 155 °C and 2 MPa for 3 min. The exact catalyst loadings were determined weighing the decal punchouts with a microbalance before and after lamination. Using a *Toray* TGP-H-120T PTFE-coated carbon fiber paper and a *Mott* 280 $\mu$m porous titanium sinter sheet as porous transport layers on cathode and anode side, respectively, the MEA was mounted into a test hardware designed and established by Bernt et al. which was introduced in detail in a former publication from our group.[2]

***Electrochemical measurements.—***Electrochemical cell testing was performed on a *Greenlight Innovation* G14 single cell electrolyzer test station supplied with $N_2$ and $H_2$ (5.0, *Westfalen*) and deionized water (18 MΩcm). The station was equipped with a *Gamry* Ref3000 potentiostat and 30K booster, and controlled via Emerald 3.0 automation software.

The cell was connected, purged with dry $N_2$ on both sides and then heated up to 40 °C while the anode was flushed with 5 ml $min^{-1}$ of water, pre-heated to cell temperature. Beginning-of-life (BoL) CVs of the anode side were recorded between 0.07 and 1.3 V at 100 $mVs^{-1}$, under liquid water at 40 °C and ambient pressure, supplying the Pt/C cathode with 50 nccm dry $H_2$. Thereafter, the cell was purged again with $N_2$ and then heated up to 80 °C, under a pre-heated water flow of 5 ml $min^{-1}$ on the anode side and an electrolysis current of 100 $mAcm^{-2}$. For conditioning of the MEA, a constant electrolysis current of 1000 $mAcm^{-2}$ was applied for 1 h at 80 °C, ambient pressures on anode and cathode, and with the same water flow as during warmup. Then three consecutive galvanostatic polarization curves were recorded from 5 to 2000 $mAcm^{-2}$ under otherwise equal conditions, whereby each current step was composed of a stabilization period of 5 min, followed by the averaging of the cell voltage over 30 s and finally an AC impedance measurement from 100 kHz to 10 Hz at a current perturbation of 10 % of its DC value. High frequency resistances (HFR) were obtained from the high-frequency intercept of the respective Nyquist plots with the real axis and used to correct polarization curves for the Ohmic drop related to the protonic membrane and electronic contact resistances. The first of these three polarization curves was considered as second conditioning step, while the latter two were regarded to represent the steady state performance at BoL, due to their perfect superimposition.

Subsequently, the simulated operation interrupt was performed in three steps, recording the cell voltage and cathode pressure over time (see Fig. 7). In the first step (*operation under pressure*), the cathode pressure was set to 5.5 $bar_a$ drawing a current of 1000 mA $cm^{-2}$, in order to build up a $H_2$ partial pressure of ~5 bar by the evolving hydrogen. In step two (*interrupt of operation*), the current was switched off together with the water flow on the anode side and the cell heating, and in the following third step (*transient period*), the cell was left at OCV for 2 h, cooling down towards ambient temperature. Thereby, no pressure was set on the anode side, i.e., the backpressure valve remained open, while the cathode set pressure was kept at 5.5 $bar_a$ ensuring that $H_2$ cannot escape through the cathode's supply or return lines. After these steps, the cell was restarted and CVs were collected the same way as at BoL. At end of test (EoT), another set of two polarization curves followed by CVs were recorded under the exact same conditions as described above.

Note that throughout the entire test protocol, the cell voltage was prevented from underrunning a value of 1.2 V, by controlling either the current (indirect) or the voltage of the cell (direct) in between the experiment sections, in order to exclude any unintended exposition of the $IrO_x$ to its open circuit potential (OCP). The only exemptions to this policy are the recording of CVs, which was kept short and at low temperature, and the simulated operation interrupt. Furthermore, the state of health of the MEA was confirmed with a leak check ($N_2/N_2$ at 5 bar vs ambient pressure) and measurement of Ohmic shorting current before and after the test procedure.

## Results and Discussion

***Reduction of $IrO_x$ catalysts in $H_2$ atmosphere.—***To verify the reducibility of $IrO_x$ predicted by the thermodynamic data summarized in Table I, two different $IrO_x$ based electrocatalysts were subjected to mass spectrometry-coupled thermogravimetric analyses (TGA-MS) under $H_2$. One sample consists of $IrO_x$ nanoparticles supported on graphitized Ketjenblack at a nominal Ir loading of 24.8 $\%_{wt}$, custom made by Tanaka Kikinzoku Kogyo (TKK),[84] called "$IrO_x$/C" throughout this work. According to TEM micrographs (cf. Fig. 1A), the catalyst is highly disperse (1−2 nm particle size) comprising amorphous, hydrous iridium oxide, as concluded from XRD and CV data (not shown).[19,20,64] The other sample is $TiO_2$ supported iridium oxide supplied by Umicore (75 $\%_{wt}$ Ir loading), an established OER catalyst for PEMWE anodes (herein called "$IrO_x/TiO_2$"). XRD reveals that the active species is mainly present in the form of crystalline $IrO_2$ (grey diffractogram in Fig. 5) and at a mean crystallite size of ~3 nm, estimated via the Scherrer equation using the main reflex' full width at half maximum (FWHM) and a Scherrer constant of 0.9. This value accords well with that reported by Alia et al. from transmission electron microscopy (TEM) analysis of the same catalyst type.[85] Its presence as thermal, crystalline $IrO_2$ is also supported by the catalyst's electrochemical surface properties (grey CV in Fig. 8) and the calcination step applied during the synthesis.[86] TEM imaging shows a rather inhomogeneous morphology without clear catalyst-support distribution (Fig. 1B) and a relatively low degree of dispersion which is

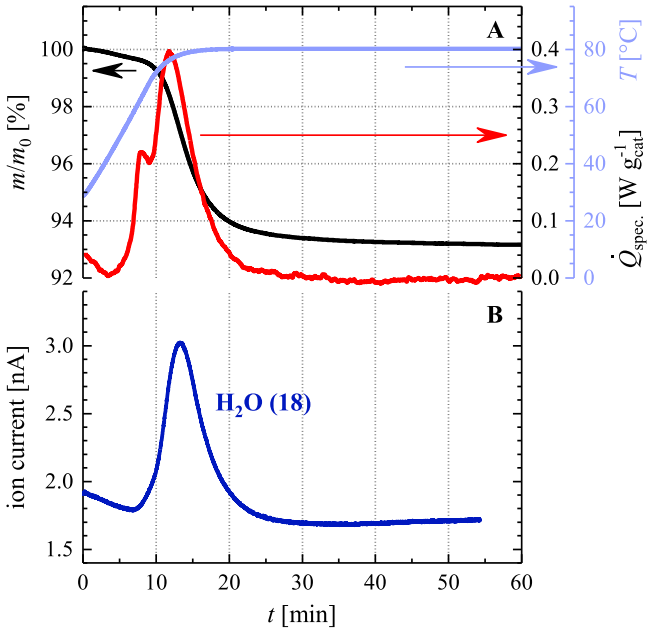


**Figure 2.** TGA-MS results of $IrO_x$/C (TKK, 24.8 $\%_{wt}$ Ir), under dynamic 5 % $H_2$ in Ar, heated from 25 °C to 80 °C at 5 K $min^{-1}$ and then held at 80 °C for 12 h (not shown entirely). (A) shows the mass loss (TGA, black), the respective heat flux, $\dot{Q}$, (DSC, red), and the sample temperature (blue) over time. (B): on-line MS data confirms the evolution of water along with the evolution of reaction heat.

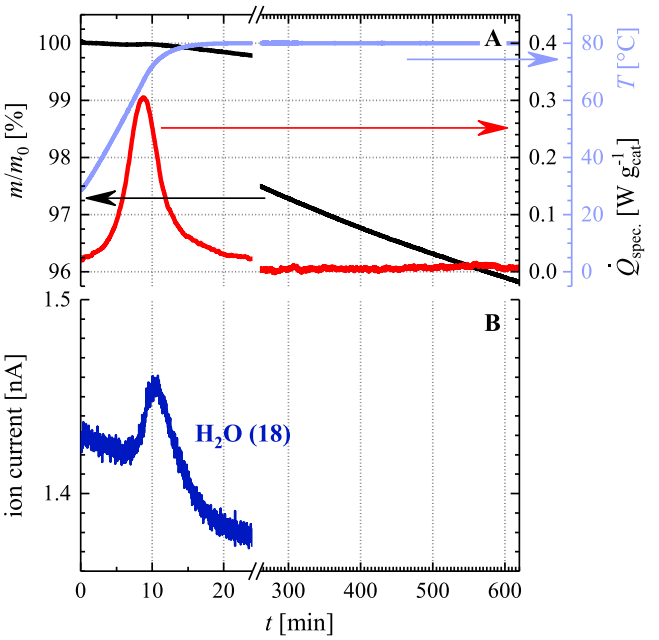


**Figure 3.** TGA-MS results of $IrO_x/TiO_2$ (Umicore, 75 $\%_{wt}$ Ir), under dynamic 5 % $H_2$ in Ar, heated from 25 °C to 80 °C at 5 K $min^{-1}$ and then held at 80 °C for 12 h (not shown entirely). (A): Curves show the mass loss (TGA, black), the respective heat emission (DSC, red) and the sample temperature (light blue) vs time. (B): on-line MS data recorded during the first 60 min confirms the evolution of water as the temperature approaches its plateau.

confirmed by its BET-determined surface area of only ~30 $m^2$ $g^{-1}$ and points at a film-structure rather than separate nanoparticles of the size indicated by the XRD mentioned above. Furthermore, EDS investigation under the TEM (results not shown) suggests that the titania support is fully covered with iridium species.

Our motivation for the choice of these two candidates was to first check the reactivity of an $IrO_x$ sample that provides the lowest possible kinetic obstacles towards chemical reduction (high dispersion and low crystallinity of the $IrO_x$/C by TKK) in order to then test the respective behavior of a state-of-the-art OER catalyst designed to sustain the harsh conditions of a PEMWE anode. While not applicable for water electrolysis, the $IrO_x$/C investigated herein typifies a possible co-catalyst for the OER in cell reversal-tolerant PEMFC anodes. On the other hand, Umicore's $IrO_x/TiO_2$ is currently deployed in both of these applications.

Figure 2 shows TGA-MS results of the thermal treatment under 5 $\%_{vol}$ $H_2$ in Ar of the $IrO_x$/C sample provided by TKK: The TGA signal (black curve) confirms a rapid mass loss between 60 °C and 80 °C, which flats out as the heating ramp approaches 80 °C, and stabilizes at ~93 % of the original mass after another 30 min at this temperature. These 7 % loss are in between the theoretical 8.8 $\%_{wt}$ and 6.5 $\%_{wt}$ of oxide and hydration water contained in a hypothetical carbon supported "$IrO_2 \times 2H_2O$" (or "$Ir(OH)_4$") and "$IrO_2 \times H_2O$" (or "$IrO(OH)_2$"), respectively, at the total Ir content of 24.8 $\%_{wt}$ given by the manufacturer. Thereby, a lower average $IrO_x$ hydration level seems more likely than an incomplete reaction at this point, since the sample mass remains stable over the subsequent 11 h under the same conditions (not shown). DSC and MS signals recorded on-line show significant formation of reaction heat and water (red and dark blue lines in Figs. 2A and 2B, respectively) evolving simultaneously with the mass loss. Hence, all results displayed in Fig. 2 point consistently at the course of the following reaction:

$$IrO_2 \times nH_2O + 2H_2 \rightarrow Ir + (2 + n)H_2O \quad [6]$$

Where the effective hydration stoichiometry n is between 1 and 2, but most probably closer to 1. The temperature at which this reduction takes place matches perfectly the 70 °C reported by Reier et al. for their (X-ray-)amorphous IROF.[29] The thermodynamics of the reaction sequence in Eq. 6 is equal to that in Eq. 1, provided that (a) liquid water is formed, (b) differences between amorphous $IrO_x$ and crystalline $IrO_2$ are neglected, and (c) the hydration water is entropic regarded as liquid $H_2O$. For the formation of gaseous water, the values in Table I need to be extended by the free evaporation energy of one equivalent of $H_2O$.

In an attempt to check for consistency between the heat emitted during the experiment and that expected from the reaction enthalpy, the DSC signal was quantitatively analysed as follows: The curve was corrected for the heat uptake of the carbon support during the temperature ramp, estimated from the temperature dependent heat capacity of graphite given in Ref. 87. The corresponding heat flux was normalized to $mol_{Ir}$ and then divided by the $\Delta_r G^T$ value of Eq. 6 at the respective temperature, as calculated via Eq. 5, yielding the conversion rate of Ir in $s^{-1}$, of which the integral over the time scale corresponds to the relative conversion. This value reaches a plateau after ~30 min at 67 % or 70 % depending on whether formation of liquid or gasiform $H_2O$ is assumed, viz., only ~2/3 of the reaction heat expected from a quantitative reduction of the hydrous $IrO_x$ is measured during the experiment, while the mass loss points at a full conversion. An evaluation of this discrepancy together with a more detailed description of the method is given below with the analogous analysis on Umicore's $IrO_x/TiO_2$ (cf. Fig. 6).

$IrO_x/TiO_2$ from Umicore was analyzed analogously applying the same heating ramp (5 K $min^{-1}$) and gas composition as before with $IrO_x$/C. The results are plotted in Fig. 3, showing very similar qualitative trends of mass loss, heat emission and water evolution as the experiment in Fig. 2, allowing for a comparable conclusion concerning the reaction taking place. Thereby, the reduction of $IrO_x/TiO_2$ is strongly retarded, but proceeds clearly over the course of the experiment, most probably to be explained by the significantly lower dispersion of this catalyst compared to the $IrO_x$/C from TKK, and also by its high degree of crystallinity (cf. grey diffractogram in

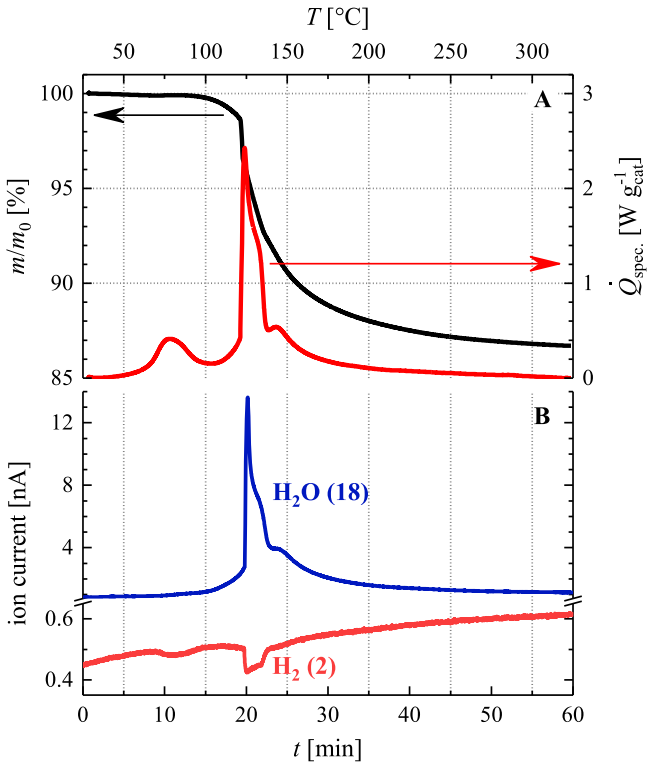


**Figure 4.** TGA-MS results of $IrO_x/TiO_2$ (Umicore, 75 $\%_{wt}$ Ir), under dynamic 5 % $H_2$ in Ar, heated from 25 °C to 325 °C at 5 K $min^{-1}$. (A) shows the mass loss (TGA, black) and the respective heat emission (DSC, red) with increasing temperature. (B): on-line MS data confirms the evolution of water and indicates even the consumption of $H_2$ simultaneously with the evolution of heat.

Fig. 5). After 10 h at 80 °C, the sample has lost ∼4 % of its original mass, corresponding to ∼1/3 of the $IrO_x$-bound oxide in the catalyst for x = 2 (i.e., 12.5 $\%_{wt}$ of a water free "$IrO_2/TiO_2$" at 75 $\%_{wt}$ Ir). The DSC signal in Fig. 3 shows a single peak of heat emission between 40 °C and 80 °C, which is, however, not accompanied by a respective mass loss in the TGA signal. A possible explanation for this feature is that it represents the early reaction of an $IrO_x$ fraction that is easy to reduce (e.g. the surface), which is then followed by the reaction of the remaining $IrO_x$ taking place very slowly at 80 °C (Fig. 3). Assuming that the water formed during the first step remains adsorbed on the sample's surface as long as the temperature is relatively low, one could explain qualitatively the delayed mass loss and water detection in the effluent gas. Note that the MS signals recorded and displayed in this study are not baseline corrected, and that they are too weak to allow for any quantitative conclusion.

The TGA-MS analysis of $IrO_x/TiO_2$ was repeated, now continuously increasing the temperature up to 325 °C under otherwise equal conditions. The results are plotted in Fig. 4, showing that compared to the previous experiment which was limited to 80 °C, the reduction of $IrO_x/TiO_2$ swings in much more abruptly at elevated temperatures (i.e. >100 °C), even causing a measurable reduction of the $H_2$ concentration in the effluent gas (cf. red trace in Fig. 4B). The total mass loss of ∼13 % fits the theoretical 12.5 $\%_{wt}$ of the $IrO_2$-bound oxide fraction in the catalyst, pointing at a reaction in the form of Eq. 1 with full conversion. This is further supported by an XRD pattern recorded after the reductive treatment in the TGA (red line in Fig. 5), which proves the transformation from an $IrO_2$-dominated composition with little content of most probably metallic Ir to an almost pure Ir (from grey to red diffractogram). The only reflex in the reduced sample that cannot be assigned to Ir is at the position of the main peak of Anatase $TiO_2$, representing a hint at the form of the titania support material which accords with

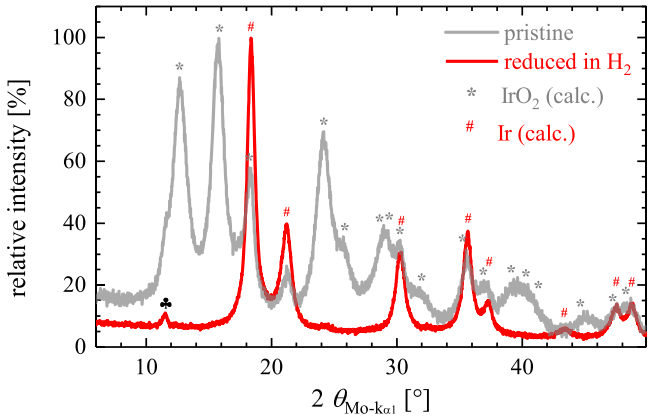


**Figure 5.** X-ray diffraction patterns of catalyst powders collected under Mo-$k_{\alpha 1}$ radiation: fresh $IrO_x/TiO_2$ catalyst (grey) vs the sample heat treated under dilute $H_2$ (red) in the TGA experiment described in Fig. 4. The most prominent reference reflection angles for $IrO_2$ (*) and Ir ($^{\#}$) are indicated with symbols, whereas the main peak position of Anatase $TiO_2$ is marked with a "♣".

Umicore's statement about "the preferred $TiO_2$ […] modification" in their respective patent.[86]

Interestingly, the reaction heat in Fig. 4A evolves in two almost fully separated steps, whereby the first peak in the DSC signal is remarkably similar to the one observed in Fig. 3. It appears between 60 °C and 100 °C, where no significant mass loss and water evolution are detected, and is comparable in shape, height and area (i.e. ∼125 and ∼140 J $g_{cat}^{-1}$ in Figs. 3 and 4, respectively). In contrast to the experiment limited to 80 °C where the further reaction takes place very slowly, the reduction of the remaining $IrO_x$ is accelerated at the now continuously elevated temperature and proceeds between 120 °C and 150 °C, i.e., considerably earlier than for the thermal $IrO_x$ film studied by Reier et al.[29] This second feature of heat emission comes along with the major drop of sample mass and with a congruently shaped water signal in the on-line MS. Moreover, the MS trace at $m/z = 2$ indicates the consumption of $H_2$ simultaneously with both features in the DSC signal. Seeking for an explanation conformable with all these observations brings us back to the aforementioned suggestion that in the first step, early and facile $IrO_x$ reduction proceeds through Eq. 1 forming liquid water, followed by the kinetically more hindered reaction of the remaining $IrO_x$ in the second step at higher temperatures and under the evolution of gasiform $H_2O$. The most conceivable representation of these two $IrO_x$ fractions is to assign them to surface and bulk, whereby the observed discrepancy in reduction kinetics would be based mainly on their different accessibility for $H_2$. If this hypothesis holds true, the ratio of ∼20/80 between the integrals of the first and second DSC feature in Fig. 4 should be a valid measure of the iridium oxide's surface-to-bulk ratio in the $IrO_x/TiO_2$ catalyst. In this respect, the paragraphs below provide a quantitative analysis of the measured DSC signal in order to answer the following questions:

I. Energetic analysis: Does the measured emitted heat cover the expected heat of reaction?
II. Morphological analysis: Provided that the heat emission profile is linked to the catalyst dispersion, as suggested above, how many monolayers (ML) of $IrO_x$ would the "surface" reduced in the first step correspond to?

For an energetic investigation, the free energy of reaction for the reduction of $IrO_x$ (approximated herein with the sequence in Eq. 1) has to be calculated as function of temperature. To account for the relatively wide temperature range of the experiment in Fig. 4, we abolished the simplification of a temperature-independent $\Delta_r c_p$ included in Eq. 5, and re-calculated $\Delta_r G^T$ via Eq. 7.

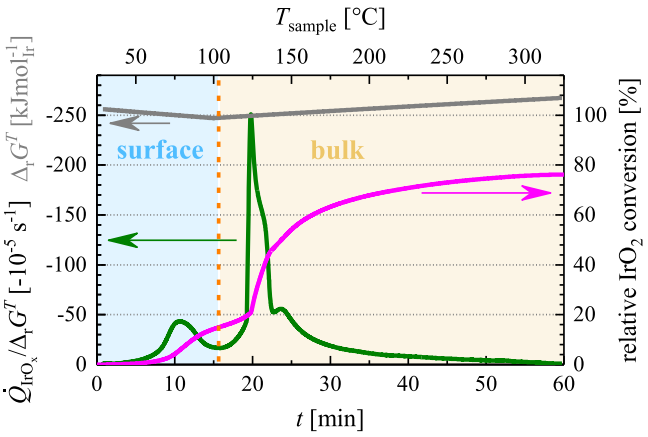


**Figure 6.** Analysis of $IrO_x$ conversion during the experiment summarized in Fig. 4. Gibbs free energy of reaction (grey line) was calculated as a function of temperature based on data available in the literature, assuming the reaction sequence in Eq. 1 forming liquid water below 100 °C, and gasiform $H_2O$ beyond. The theoretical conversion rate (green line) is obtained as quotient between the corrected DSC signal and $\Delta_r G$, and the time integral corresponds to the theoretical $IrO_2$ conversion (magenta line).

$$\Delta_r G^T = \Delta_r H^\circ + \Delta\Delta_r H^{298K\rightarrow T} - T \cdot (\Delta_r S^\circ + \Delta\Delta_r S^{298K\rightarrow T}) \quad [7]$$

Thereby, the changes of reaction enthalpy and entropy with temperature ($\Delta\Delta_r H$ and $\Delta\Delta_r S$, respectively), can be calculated from the function of $\Delta_r c_p(T)$ through Eqs. 8 and 9.

$$\Delta\Delta_r H^{298K\rightarrow T} = \int_{298}^{T} \Delta_r c_p(T)\, dT \quad [8]$$

$$\Delta\Delta_r S^{298K\rightarrow T} = \int_{298}^{T} \frac{\Delta_r c_p(T)}{T} dT \quad [9]$$

To estimate $\Delta_r c_p(T)$, $c_p$ values of all reactants tabulated for the temperature range of interest were taken from Refs. 82, 87, 88, fitted to a polynomial function in the form of Eq. 10,

$$c_p(T) = a + bT + cT^{-2} + dT^{-0.5} \quad [10]$$

Where $a$, $b$, $c$ and $d$ are fitting parameters with different units. The functions of $c_p(T)$ were then summed up considering their respective stoichiometry to yield $\Delta_r c_p(T)$. Note that our calculations are based on values for hydrogen and water vapor at standard pressure, neglecting the dilution of the $H_2$ feed with argon and the eventual mixing of reactant gas with product water.

As stated earlier, our hypothesis that in the first reduction step, liquid water is formed and remains adsorbed on the catalyst surface, is to accommodate the observed absence of simultaneous mass loss as well as the insufficient detection of $H_2O$ in the exhaust gas. Hence, we assumed that the evaporation of this fraction of $H_2O$ proceeds at the transition between first and second step around 100 °C, where the free evaporation energy of water ($\Delta_{vap}G$) is approximately zero, and therefore can be neglected in this analysis. The DSC curve was normalized to W mol$_{Ir}^{-1}$ after correction for the heat uptake of the $TiO_2$ support upon heating (based on $c_p(T)$ of anatase estimated from Ref. 87), and then divided over the temperature scale by $\Delta_r G(T)$ (in J mol$_{Ir}^{-1}$, grey line in Fig. 6) for liquid or gaseous $H_2O$ below and above 100 °C, respectively. The resulting relative conversion rate in s$^{-1}$ (green line in Fig. 6) was finally integrated over the time scale yielding the relative $IrO_x$ conversion given in % in Fig. 6 (magenta line). Surprisingly, only ~75 % of the expected reaction heat was measured throughout the experiment, which is most probably not due to an incomplete reduction, backed up by the measured mass loss as well as by the subsequently recorded XRD. Also the calculated $\Delta_r G^T$ is reasonably precise. The most conceivable source of this discrepancy is the insufficient precision of the DSC tool, which operates under a continuous gas flow in the TGA instrument, contrary to normal DSC experiments. In this respect, a certain heat dissipation through the reactant and carrier gases must be expected when the sample temperature exceeds that of the furnace due to heat evolution, which is not accounted for by the applied conventional background correction. Note that such deviation was already observed to a similar extent in the experiment drawn in Fig. 2. In addition, the XRD pattern of the pristine catalyst (grey line in Fig. 5) shows that the Ir content of 75 % is not exclusively in the $IrO_2$ form, as was supposed in the analysis above, but seems to have a smaller fraction in the metallic state. Assuming that 10 % of the original Ir is metallic, the measured heat would cover 85 % instead of 76 % of the theoretical value, whereby the expected mass loss of 11.2 % would still be reasonably close to what was measured in TGA. Furthermore, a certain content of $H_2O$ in the sample, in the form of either adsorbed water or hydrous oxide, cannot be excluded from our characterization, and would emerge as lower heat emission with at the same time higher mass loss. Regarding these uncertainty factors, we can conclude that the heat emitted from the $IrO_x/TiO_2$ sample heat treated under $H_2$ is roughly covered by the theoretical heat of reduction of its $IrO_2$ content to metallic iridium.

Since the variation of $\Delta_r G^T$ with temperature is relatively weak, the conversion rate curve is qualitatively similar to the DSC signal and consequently, the 1st peak's share in total conversion should be 20 %, as is the fraction of heat under the 1st DSC feature. As mentioned above, these 20 % could represent the surface-to-bulk ratio of the $IrO_x$ in the catalyst sample, wherefrom the average surface layer thickness shall be estimated in the following analyses, assuming that the catalyst's exterior surface (i.e., the BET-determined surface area) consists exclusively of $IrO_x$, and that the 75 %$_{wt}$ Ir are fully in the dioxide form.

In a first approach, the catalyst's morphology is simplified by a film model, i.e., a uniform $IrO_x$ film atop a flat anatase substrate, so that the thickness of the $IrO_x$ film is obtained as the reciprocal of the product from BET area and the density of $IrO_2$ yielding 2.50 nm. The 20 % thereof assigned to the "easy to reduce" $IrO_x$ surface layer (0.50 nm) would correspond to 1.6 MLs of $IrO_2$, estimated via the average ML thickness obtained as cubic root of the "molecular volume," i.e., the molar mass divided by the density and the Avogadro constant. The second approach accounts for the factual surface curvature of the catalyst assuming monodisperse core-shell particles, i.e., equally sized spheres of $TiO_2$ covered with a uniformly thick mantle of $IrO_x$. The thickness of the latter is calculated as 3.54 nm, of which the outermost 20 % of substance correspond to a 0.53 nm thick shell or 1.7 MLs of $IrO_2$. Note that the number of given digits shall not connote a respective experimental precision. In fact, we intend to emphasize that the results calculated with the two described film models are quasi equal. Hence, these results allow not only for the conclusion that the reduction of the catalyst's active material starts with the topmost 1–2 MLs of $IrO_2$, but demonstrate as well that differences in the obviously quite irregular morphology have a relatively weak impact on the outcome of the assessment. It is likely, though, that unsupported $IrO_x$ fractions of higher dispersion degree get reduced to a larger extent, while on other domains only the surficial ML undergoes a reaction in the 1st step. Altogether, we gained further support for our assumption that the observed two steps of heat emission can be assigned to the subsequent reduction of surface and bulk $IrO_x$ in the investigated catalyst sample.

In summary, the reduction of thermal $IrO_x$ (herein represented by Umicore's Elyst Ir75 0480, $IrO_x/TiO_2$) can be considered not only thermodynamically, but also kinetically possible under the conditions of an operating low-temperature PEMFC anode. Thereby, the surface fraction reacts quickly (likely within minutes), while the full reduction of the bulk material takes much longer. It is obvious that $IrO_x$ added as co-catalyst to PEMFC anodes in an attempt to mitigate

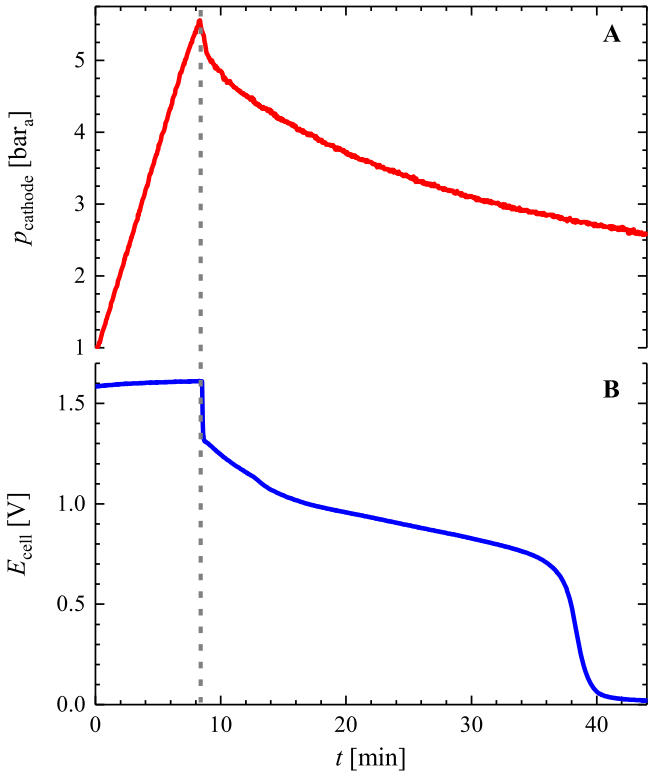


**Figure 7.** Transients of cathode pressure (A) and cell voltage (B) during the conducted operation interrupt test. The cell was operated at 80 °C, ambient pressures and 1000 mA $cm^{-2}$. At the origin of the displayed time scale, the cathode pressure was set to 5.5 bar, then the current was shut off as well as the water supply and heating of the cell (i.e. operation interrupt, as marked by the dashed vertical line).

degradation during cell reversal, will be transformed into metallic Ir on a relatively short timescale. Since the latter is much more prone to dissolution under potential transients,[46] our finding ultimately questions the co-catalyst's mitigation effectiveness over the lifetime of a fuel cell.

***$H_2$ crossover in a PEMWE MEA.***—After demonstrating that thermal iridium oxides can get fully reduced under $H_2$ at the typical operation temperature of PEMFCs, we want to illustrate the relevance of this knowledge for PEM electrolyzers, where $IrO_x$-based catalysts are commonly used to catalyze the evolution of $O_2$ in the anode. Since the typical operation temperature is fairly similar to that of a PEMFC, the pivotal question thereby is how the anode can possibly get in contact with $H_2$. Such scenario is actually quite easy to draw considering the relatively high gas permeability of PFSA membranes:[89,90] Analogously to the well-known $H_2$ crossover from anode to cathode in PEM fuel cells, hydrogen permeates through the membrane of PEMWE devices from the $H_2$-evolving cathode into the anode compartment.[91] Since due to economic aspects, PEMWEs are usually operated at elevated $H_2$ pressures (recent plant-level estimates predict an optimal operating cathode pressure to 20–50 bar),[92] these permeation rates can amount to several 10 s of mA $cm^{-2}$, depending on the membrane type and thickness.[90] This aspect is generally considered a safety and/or efficiency concern[93] but usually not with respect to catalyst durability, because as long as the cell is under operation, the high anode potential of >1.4 $V_{RHE}$ should hinder the $IrO_x$ from any reaction with $H_2$ and ultimately conserve its high oxidation state and thereby corrosion resistance. However, steady operation can hardly be presumed over the device's entire lifetime, taking into account periods of shutdown due to maintenance or intermittent electricity interruptions especially for grid-implemented electrolyzers supplied by fluctuating renewable energy power plants. Without suitable mitigation strategies, such transient conditions would cause extended open circuit voltage (OCV) periods during PEMWE operation, under which the $IrO_x$ in the anode might undergo a reaction with $H_2$ analogously to what was described above. To the best of our knowledge, our study has been the first one reporting the effect of such OCV periods in combination with $H_2$ crossing over from the cathode compartment.[94]

For respective experimental investigation, we designed an easy 3-step protocol to mimic "operation interrupt" events in a PEMWE cell at elevated $H_2$ pressure, which comprises pressurization of the cathode compartment with electrochemically evolved $H_2$, switch-off of the cell current and heating (i.e., operation interrupt), and a 2 h delay period under OCV. The test was conducted on a PEMWE MEA with 5 $cm^2$ active area (see experimental section for details on cell assembly and testing conditions) and the development of cathode pressure and cell voltage throughout the three experiment steps is plotted in Figs. 7A and 7B, respectively, with the mimicked operation interrupt marked by the vertical dashed line. The pressure profile displays as expected a steady pressurization under the initial HER current of 1000 mA $cm^{-2}$, followed by an exponential-like decline after the evolution of $H_2$ was interrupted. Note that during this period the cathode's supply and return lines were kept closed, and that the assembled cell hardware had been subjected successfully to a tightness test at 50 bar of helium, when it was established for use in our labs.[2] Hence, any leakage of gas from the pressurized cathode compartment can occur exclusively via diffusion through the membrane to the anode side, which was kept at ambient pressure through an open backpressure valve. For verification, we calculated the corresponding gas leak rate as derivative of the measured pressure transient via the estimated volume of the pressurized cathode compartment. The result is relatively constant over time (ca. 0.06 $nccmbar^{-1}$), and greatly consistent with the $H_2$ crossover current of 1.6 A $cm^{-2}bar_{H2}^{-1}$ measured in our labs on fully humidified Nafion 212.

On the other hand, the voltage trend shows an interesting pattern: Starting out around 1.6 V, corresponding to the drawn electrolysis current, the cell voltage increases slightly with elevating $H_2$ pressure at the cathode (~30 mV expected with the rise from ~0.5 to 5 $bar_{H2}$), to then fall immediately to the thermodynamic equilibrium around 1.2 V as the current is switched off. Subsequently, the voltage drops quickly below 1 V, reaches a sloped plateau and finally falls to a value slightly above 0 V, which slowly approaches 0 V over the rest of the 2 h OCV period (not entirely shown). Considering that the cathode is situated at an RHE potential that varies only marginally with the dropping $H_2$ pressure after the operation interrupt, the characteristics of the observed voltage profile must be assigned to the anode potential and the processes taking place on the $IrO_x$ catalyst surface. Therefrom, two questions are arising: a) which electrochemical equilibria hold the electrode at the plateau around 800 $mV_{RHE}$, and b) what happened to the $IrO_x$ surface, that it could finally stabilize at 0 $V_{RHE}$? After the cell is switched to OCV, no more oxygen is evolved and the remaining $O_2$ in the anode compartment gets continuously diluted by the $H_2$ crossing over from the cathode side, or diffuses through the membrane. While oxygen will immediately recombine with $H_2$ on the cathode's Pt surface, depletion of $H_2$ on the anode side can initially be neglected due to the inactivity of $IrO_2$ towards the HOR.[95] At some point, the anode atmosphere will be dominated by hydrogen fulfilling the conditions for the reduction of $IrO_x$ to proceed *chemically* pursuant to Eq. 1 as it was observed in the TGA experiment plotted in Fig. 3. Furthermore, the *electrochemical* reduction along Eqs. 2 and 3 should become possible as soon as a minimum of HOR active species is present on the surface, which would be the case once the first Ir sites have formed. With these reactions running, the electrode potential would be located around the equilibrium potential of Eq. 2, fading out with propagating reduction depending on the particular ratio between $IrO_x$ and Ir species on the surface. However, the equilibrium potential of the electrochemical reduction of $IrO_x$ calculated in Table I is ~150 mV

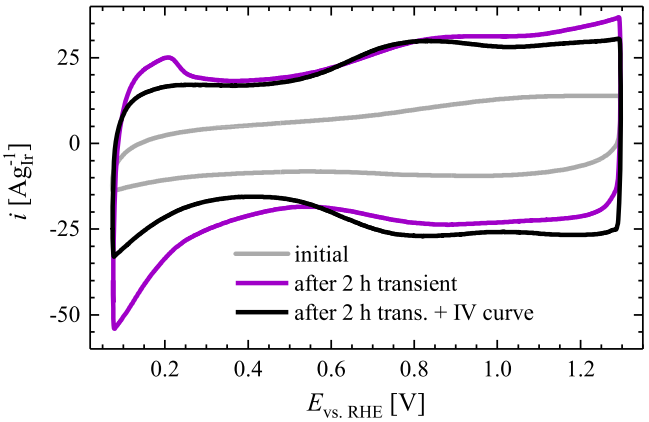


**Figure 8.** Cyclic voltammograms recorded at 40 °C, 100 mVs$^{-1}$, and under liquid $H_2O$ on a 5 cm$^2$ PEMWE anode loaded with $IrO_x/TiO_2$. The grey CV represents the initial state of a thermal oxide with nearly pure double layer capacitance. Further CVs were recorded directly after one 2 h OCV period (purple) and after a polarization curve recorded thereafter (black).

lower than the potential plateau measured in our operation interrupt tests (Fig. 7B). This may be due to a positive impact of the remaining $O_2$ on the mixed anode potential, considering the moderate ORR activity of Ir that would cause an open circuit potential (OCP) around 0.9 $V_{RHE}$ as was reported for an Ir/C-based electrode.[96] Moreover, it was stated in the literature that present $O_2$ has an effect on the degree of hydration of the iridium oxide,[97] which could change the thermodynamics of Eq. 2 and thereby as well lead to an additional shift of the overall equilibrium potential. By the time the surface $IrO_x$ has been depleted, the anode potential will eventually drop to the RHE thanks to the available Ir sites under $H_2$ atmosphere.

Interestingly, we initially observed PEMWE cell voltage transients shaped like the one plotted in Fig. 7B during unintended potentiostat outage (leaving the cell at OCV) in the course of electrolysis tests in our lab. Thereby, the time interval until the cell approached ~0 V scaled inversely with the $H_2$ pressure in the cathode compartment as well as with the temperature of operation, and shortened significantly for subsequent OCV periods. Together with the TGA/DSC analyses presented above, these findings gave the motivation for the detailed analysis herein. Meanwhile, a follow-up investigation from our group has been published analyzing the effect of OCV periods further, focusing on lifetime durability concerns for PEMWEs.[98] The cell voltage transient observed therein accords qualitatively with the one plotted in Fig. 7, though the anode's OCP reaches the RHE potential within only ~10 % of the time (i.e., ca. 3 min instead of the 30 min herein). This acceleration of the effect is most likely due to a couple of experimental discrepancies, which reflect the different approaches of the two studies. Thereby, the twofold $H_2$ pressure in the cathode and the higher temperature during the tests in Ref. 98 probably make up the key difference, simply because our TGA experiments above have shown that the reduction of $IrO_x$ in $H_2$ is strongly kinetically limited, especially below 100 °C.

We want to point out that a similar potential profile has been reported before in a similar context by Brightman et al., who investigated the OCV of a PEMWE cell in shut down periods during power cycling.[99] They recorded a sudden cell voltage drop to ~1.2 V as the current was switched off, followed by a first plateau around ~1 V fading out into a second plateau at ~0.3 V. With the help of an independent reference electrode they disentangled the transients of anode and cathode potentials from each other, revealing that the cell voltage profile was dominated by the 2-stepped increase of $E_{cathode}$ towards ~0.9 $V_{RHE}$, while the anode asymptotically approached a potential of ~1.2 $V_{RHE}$ without any distinct features. We suggest the following explanation: when the current is interrupted, the anode and cathode compartments are filled with $O_2$ or $H_2$, respectively, which diffuse along their individual concentration gradient across the membrane. At the cathode's Pt surface, they react at a ratio of 1:2 to form water, viz., the concentration of $H_2$ decreases twice as fast as that of $O_2$ and consequently approaches zero, provided that the cell was operated at balanced pressure, which is at least not otherwise stated.[99] In how far this use-up of gas molecules is balanced by ingress of air from the atmosphere or by a continuing water feed, cannot be answered on the basis of their experimental section. It appears logical though, that sometime after shutdown, the cathode potential becomes predominantly controlled by $O_2$ causing an OCP close to 1 V, which is covered by their results and also discussed accordingly. On the other hand, Brightman and coworkers conclude from the distinctive stability of their anode potential, that the used $IrRuO_x$ catalyst is "relatively insensitive to $H_2$," without giving an indication of how an alternative sensitivity to $H_2$ could be featured. However, this statement would require that $H_2$ accumulates to a sufficient extent on the anode side, which is not likely in their cell supposing an operation at balanced pressure. In contrast, our test was carried out at a $H_2$ pressure of 5 bar vs only ~0.5 bar $O_2$. Accordingly, through the above-described mechanism of gas depletion while the cell is at OCV, hydrogen prevails in our cell on both sides of the membrane, maintaining a stable RHE potential of the cathode, while the anode catalyst is exposed to a more and more reductive atmosphere and incrementally vanishing $O_2$ concentration. The latter is further enhanced due to squeeze-out through our open anode outlet, eluding the intruding hydrogen. Significant discrepancies originating from the different anode catalysts are unlikely, because the reduction of $RuO_2$ with $H_2$ is almost as exergonic as that of $IrO_2$.[12]

***Operation interrupt: effect of OCV period on catalyst surface properties and OER activity.—***In order to understand the processes taking place on the anode surface during the described operation interrupt test, CVs and polarization curves were recorded at beginning of test and after the OCV period. The initial anode CV (grey in Fig. 8) shows no distinct features but the bare double layer capacitance expected for a thermal iridium oxide.[2,31] After the OCV period, the $IrO_x$ surface properties have changed significantly as obvious from the CV recorded directly thereafter (purple in Fig. 8): H-UPD features and grown HER activity hint at metallic Ir on the surface and grown, reversible oxide redox features between 0.5 and 1.2 V can be dedicated to hydrous $IrO_x$.[19,20] Interestingly, the metallic surface characteristics seem to vanish during the subsequent polarization curve, while the evolved oxide redox capacity is retained, as depicted by another CV recorded after that latter IV plot (CV in black in Fig. 8). Hence, the original state of the thermal $IrO_x$ cannot be recovered under the high anodic polarization during the IV plot, indicating an irreversible transformation to a more hydrous $IrO_x$ throughout the conducted reduction-reoxidation cycle (grey to black CV). This is, however, limited to a certain fraction of the $IrO_x$ in the catalyst layer (i.e., most likely its surface), considering the still remarkable capacity in the black CV below 0.5 V. In this potential range, fully hydrated Ir oxides are in the reduced Ir(III) state and contribute very marginally to the CV's capacitive current, which on its part mainly originates from the substrate below the hydrous $IrO_x$ (i.e., e.g. metallic Ir or dry $IrO_2$).[19,20,28,36,64] Consequently, the significant capacity growth at <0.5 V from the grey to the black CV points at residual Ir surface below the formed hydrous $IrO_x$ film or at a surface roughening of the thermal $IrO_x$ substrate during the formation process of this film.[65,100] The trend of the electrochemical anode catalyst surface properties qualified by the three CVs in Fig. 8 was also well reproduced in the aforementioned follow-up study from our group and explained accordingly.[98]

For a better evaluation of the observed development of metallic Ir surface properties, another MEA of the same type was subjected to a longer reductive treatment instead of the mimicked operation interrupt test that lead to the purple CV in Fig. 8: Anode and

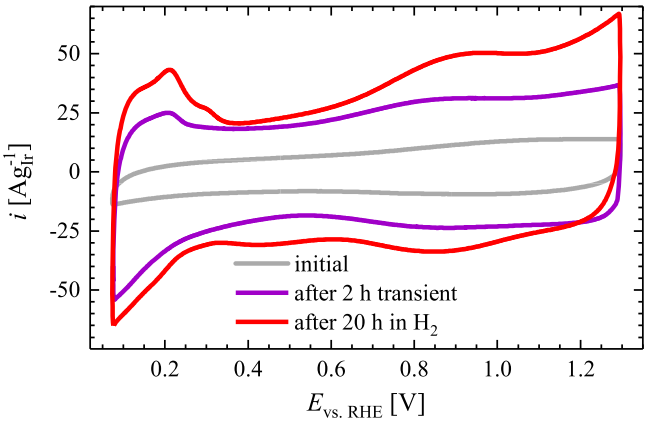


**Figure 9.** Comparison of CVs shown in Fig. 8 with that recorded on an $IrO_x/TiO_2$ electrode after 20 h exposition to pure $H_2$ at 80 °C (red, partial reduction to metallic Ir confirmed by XRD). The reductive treatment leading to the CV in red was done on an as-assembled MEA inside the cell hardware.

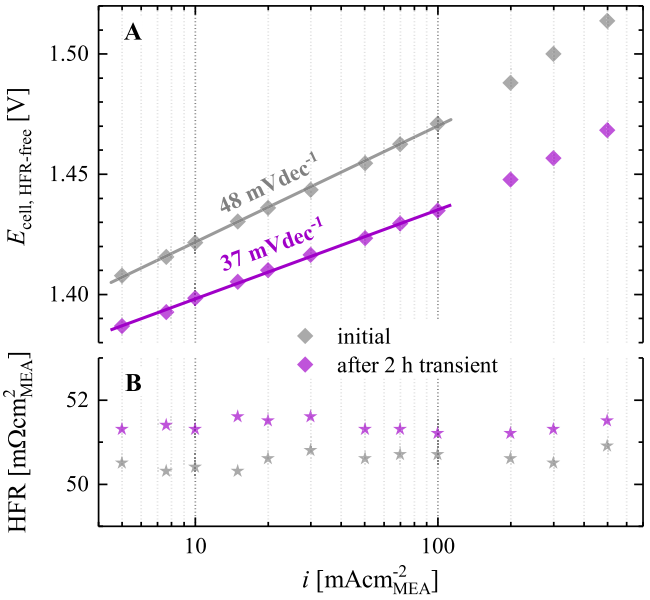


**Figure 10.** Tafel plots of polarization curves (A) at initial state (grey), and after one 2 h OCV period (purple). IV plots were recorded galvanostatically at 80 °C and ambient pressure on a MEA with 5 $cm^2$ active area, fed with 5 ml $min^{-1}$ liquid $H_2O$ to the anode. HFR values estimated from impedance spectra recorded during the IV plots are displayed in (B).

cathode were supplied with pure, fully humidified $H_2$ at 80 °C, and the cell was left at OCV for 20 h. The subsequently recorded CV is plotted in Fig. 9 (in red) together with those discussed above, showing more strongly developed H-UPD and oxide redox features compared to that collected after the operation interrupt test (purple CV). Its overall shape is similar to those reported for metallic iridium electrodes,[19,64,70] whereby an additional impact of present hydrous iridium oxide to the capacitive current appears likely.

Polarization curves were recorded before and after the operation interrupt test and are plotted in Fig. 10 following the same color code used above for the CVs. The initial curve shows linear Tafel behavior up to 100 mA $cm^{-2}$, at a Tafel slope of 48 mV $dec^{-1}$ indicating kinetic limitation from the OER. This is in perfect agreement with our previously published data measured with the same OER catalyst and using an equal cell setup and hardware.[2] After the OCV period, the Tafel plot is still linear up to 100 mA $cm^{-2}$, but at a significantly reduced slope of 37 mV $dec^{-1}$, and a strongly increased OER activity, as expressed by a 20–30 mV decrease in overpotential in the kinetic region. Divided by the Tafel slope, this corresponds to a ~1/2 decade higher (i.e., ~3-fold) OER kinetics in the respective overpotential range. These trends in kinetic overpotential and Tafel slope are both in good accordance with the polarization curves reproduced with similar experiments in another study from our labs.[98] Assigning this activity boost to the transformation of the anode catalyst surface from a dry, crystalline to a more hydrous $IrO_x$, as concluded from the recorded CVs (cf. Fig. 8), would be qualitatively very well consistent with previous studies.[23,27–31] The Tafel slope drop is also in line with literature: Gottesfeld et al. observed the same trend comparing the OER of an Ir electrode covered with a thick hydrous $IrO_x$ layer to that of the same electrode after anodic dissolution of this layer (experiments in liquid electrolyte).[23] This was confirmed later and analyzed in more detail by Vukovich, who subjected hydrous $IrO_x$ films to thermal treatment and reported a systematic increment of the OER Tafel slope with the annealing temperature.[27] The same correlation was verified in several recent papers,[29,30,56] and approved as well with polymeric electrolytes.[47,48] These trends have strong implication for the dominant OER mechanism: On the one hand, the drop in overpotential can be assigned to the increased accessibility of Ir sites in the porous, hydrous oxide layers, which has been demonstrated by the positive correlation between capacitive charge and OER activity of $IrO_x$ electrodes calcined at different temperatures.[30,56] On the other hand, the decrease in Tafel slope is indicative of a change in the rate determining step (rds). This was discussed in detail by Gottesfeld and Srinivasan for $IrO_x$,[23] as well as for $RuO_x$ by Trasatti and coworkers.[101] The findings were justified with a surge of oxide defectives along with the decreasing crystallinity, which were expected to have a higher affinity for adsorbed OH intermediates. An analogy between the oxides of Ru and Ir can be drawn based on their remarkable similarities with respect to structure, morphology and formation of crystalline vs hydrous oxides as well as their OER activities.

Interestingly, Rakousky et al. reported also a positive effect of power shutdown periods on the performance development of PEM water electrolysis devices, which is, however, substantially different from our observations. In a recent paper, they showed that their cells suffered from a severe performance loss of >100 $\mu Vh^{-1}$ when operated at 2 A $cm^{-2}$, which could be partially mitigated by periodical interruption to the electrolysis current.[102] The authors majorly assigned the observed degradation to the oxidation of the titanium PTL at high anode potentials, increasing the contact resistance between anode and PTL and releasing Ti ions into the MEA. The latter was supposed to evolve kinetic and further Ohmic losses through poisoning of the anode catalyst as well as $H^+$ exchange groups in the polymer electrolyte. Rakousky and coworkers assume that the observed recovery in cell performance during the applied operation interruptions results from a reversion of these poisoning effects and enhances the overall cell durability. In contrast, we observed herein a sustainable and reproducible gain in OER activity leading to lower cell voltage and Tafel slope. Moreover, their post-mortem analysis shows that the $IrO_2$ particle size remained constant throughout the experiment and does not hint at $IrO_x$ dissolution or conversion into hydrous oxide. Even though Rakousky et al. did not analyze the development of cell voltage during the operation interrupt, a phenomenon similar to our reductive $IrO_x$ transformation is highly unlikely. This can be stated considering that they operated at ambient pressure, wherefore the atmosphere in the electrode compartments should eventually be dominated by $O_2$ rather than $H_2$, as explained before.

Regarding studies available in the literature, our findings have implications to PEMWE durability. In several analyses, the corrosion resistance of different iridium oxides during oxygen evolution or upon cycling in the OER potential range was found in half cell tests to develop rather oppositely to their activity trend.[30,31,46] Moreover, the higher vulnerability of hydrous oxides towards dissolution is even topped by metallic iridium,[46,70] which we expect

to be formed on the catalyst surface during exposure to $H_2$ at OCV. Provided that this stability trend holds true in polymer electrolyte full cell tests, of which the confirmation is still vacant in literature, we have reason to assume that operation interrupt events similar to the OCV test investigated herein, can be highly detrimental to the long-term durability of PEMWE anodes. This issue would become very prominent when the dispersion of $IrO_x$ catalysts is increased to reduce Ir loadings significantly below the current values of some $mg_{Ir}$ per $cm^2$, which is inevitable for a wide-spread commercialization due to the strongly limited abundance of iridium in the earth crust.

Consequently, further investigation building on our results is necessary to evaluate their relevance for the durability of PEMWE devices. Thereby, special focus should be on the effect of repetitive cycles of operation and interrupt, to accommodate the life cycle stress for electrolyzers powered with intermittent electricity sources such as wind and solar plants. Our results indicate that single OCV periods that are limited in temperature and duration, affect only the surface of Umicore's relatively low-disperse $IrO_x$ catalyst, whereby the respective boost of OER activity causes an overall increase of electrolysis performance. However, with subsequent operation interrupts, the transformation of thermal $IrO_x$ could expand into the particle cores changing not only their dissolution resistance but as well their OER activity. Preliminary data from our lab (not published) showed a consecutive shortening of the OCV's residence time at the plateau around 0.8 V (cf. Fig. 7B), in order to almost fully vanish after several 10 s of OCV periods, i.e., the anode OCP falls to $\sim$0 $V_{RHE}$ within seconds. This hints at an increasingly fast reduction of Ir at the surface, probably due to fading of the stabilization effect from the bulk $IrO_x$ core to its surface. Furthermore, higher cell temperature and cathode $H_2$ pressure can be expected to accelerate the transformation of thermal Ir oxides into less corrosion stable, hydrous $IrO_x$.

A consecutive study was conducted in our group investigating the herein described effect in a lifetime perspective, performing multiple subsequent OCV periods alternated with high- and low-power electrolysis operation in a single PEMWE cell to mimic an electrolyzer supplied with highly fluctuating and intermittent electricity supply.[98] In fact, losses evolving from the converted $IrO_x$ species on the catalyst surface were found to overcompensate soon the initial activity gain demonstrated here in Fig. 10. These are, however, not majorly related to a continuous dissolution of hydrous $IrO_x$ and respectively deteriorating OER kinetics, but show up as significant and continuous increase of the cell's HFR. A deeper analysis of different loss terms contributing to the HFR concludes that the most likely reason is the continuously increasing electronic resistance between the anode sided CL and PTL, suffering from the lower electronic conductivity of hydrous Ir oxide compared to dry $IrO_2$ and from propagating corrosion of the PTL surface. This makes clear that the lower dissolution resistance of hydrous $IrO_x$ is by far not the only issue coming up with the transformation of the OER catalyst surface under the operation interrupt events described herein.

Hence, effective mitigation strategies would be required to prevent such transients in PEMWE operation. A conceivable method for single cell testing is to hold the cell voltage around the thermodynamic equilibrium of $\sim$1.2 V during idle periods, as we did in this work. This is, however, not applicable to a PEMWE stack. On the other hand, drawing a small electrolysis current would be far easier to regulate, but requires auxiliary power and also involves the danger that an explosive $H_2/O_2$ mixture forms in the anode compartment as long as the current density is below a critical level.[95,103,104] Instead, releasing the $H_2$ pressure and/or to purge the cathode compartment with nitrogen when the electrolyzer operation is interrupted could be more effective, especially when these periods are longer. Appropriate analyses would be required to assess in how far this approach might be practical from an economic point of view.

## Conclusion and Outlook

This study gives new insights into the (electro-) chemical stability of iridium oxides under hydrogen atmosphere and demonstrates the relevance of these findings for the durability of PEM water electrolyzers.

In the first part, we showed via TGA experiments that a state-of-the-art $IrO_x$ based OER catalyst gets chemically reduced to metallic Ir when heated in a $H_2$ containing atmosphere. While heating to $>$150 °C leads to a full reduction within minutes, the reaction is strongly decelerated holding at a typical PEMWE operation temperature of 80 °C, however, at least a surficial reduction can be achieved rapidly.

To link this observation to PEMWE operation, we drew an interruption scenario where an electrolyzer is switched from an average duty point at elevated $H_2$ pressure in the cathode compartment into an idle mode where no current is applied (OCV). Thereafter, $H_2$ crossing over the membrane to the anode side should reduce chemically the $IrO_x$ surface analogously to the TGA experiment, since the catalyst is no longer stabilized by the commonly high anode operation potential of $>$1.4 V. Consequently, we tested the effect of such an operation interrupt event in a 5 $cm^2$ PEMWE single cell, starting out from operation at 80 °C, 1000 mA $cm^{-2}$ and a cathode $H_2$ pressure of 5 bar. The OCV value of the cell shows a characteristic and reproducible transient which stabilizes close to 0 V within tens of minutes, giving a strong hint at the formation of Ir sites at the anode catalyst surface which would drag the anode towards the RHE potential under the present $H_2$. This is supported by CVs recorded on the anode after a total of 2 h at OCV, which show the evolution of H-UPD as well as oxide formation and reduction features. Interestingly, upon consecutive polarization to high potentials, the catalyst surface is reoxidized to a more hydrous $IrO_x$, of which the CV significantly differs from the originally $IrO_2$-like structure. Together with a strong enhancement of the anode's OER activity (by $\sim$1/2 Tafel slope compared to its initial activity), our data consistently points at an irreversible transformation of the $IrO_x$ surface from a dry to a more hydrous oxide[29–31,64] during the encountered reduction—reoxidation cycle.

Events similar to the operation interrupt tested herein can be expected to take place numerous times within the lifetime of an electrolyzer, especially when implemented into an electricity grid with highly fluctuating power supply. Considering the fact that hydrous $IrO_x$ is on the one hand much more prone to corrosion in the OER potential region and on the other hand electronically less conductive compared to its dry $IrO_2$ counterpart,[30,31,37] the finding of this study must also be regarded as potential degradation mechanism in PEMWE operation. Performance losses can arise from cationic poisoning of the polymer electrolyte (likely not relevant with Ir in PEMWE MEAs),[105] increased electronic resistance in the anode and at its interface,[98] and a higher OER overpotential along with a degradation of the active surface area. The latter kinetic effect can become limiting especially in novel anode concepts with ultra-low $IrO_x$ loading.

## Acknowledgments

First and foremost, the authors are very grateful to Hubert A. Gasteiger for his vast contribution to this study. We acknowledge funding from Greenerity GmbH through a subcontract co-funded by the German Federal Ministry for Economic Affairs and Energy (project "HyMotion5-Brennstoffzellenstapel"). Sincere thanks go to Matthias Binder, Christian Eickes, and Peter Suchsland from Greenerity GmbH for fruitful discussions. Furthermore, P. J. R. greatly acknowledges Yasin Incedag for his works and scientific input during an early state.

## ORCID

Philipp Jan Rheinländer https://orcid.org/0000-0002-0018-065X

## References


1. K. A. Lewinski, D. F. van der Vliet, and S. M. Luopa, *ECS Trans.*, **69**, 893 (2015).
2. M. Bernt and H. A. Gasteiger, *J. Electrochem. Soc.*, **163**, F3179 (2016).
3. D. N. Buckley and L. D. Burke, *J. Chem. Soc. Faraday Trans. 1 Phys. Chem. Condens. Phases*, **72**, 2431 (1976).
4. S. Trasatti, *Electrodes of Conductive Metallic Oxides, Part B* (Elsevier Science Ltd., Amsterdam) (1981).
5. E. Fabbri, A. Habereder, K. Waltar, R. Kötz, and T. J. Schmidt, *Catal. Sci. Technol.*, **4**, 3800 (2014).
6. U. Babic, M. Suermann, F. N. Büchi, L. Gubler, and T. J. Schmidt, *J. Electrochem. Soc.*, **164**, F387 (2017).
7. D. N. Buckley, L. D. Burke, and J. K. Mulcahy, *J. Chem. Soc. Faraday Trans. 1 Phys. Chem. Condens. Phases*, **72**, 1896 (1976).
8. S. Cherevko et al., *Catal. Today*, **262**, 170 (2016).
9. C. C. L. McCrory, S. Jung, J. C. Peters, and T. F. Jaramillo, *J. Am. Chem. Soc.*, **135**, 16977 (2013).
10. O. Diaz-Morales, I. Ledezma-Yanez, M. T. M. Koper, and F. Calle-Vallejo, *ACS Catal.*, **5**, 5380 (2015).
11. S. Trasatti, *Electrodes of Conductive Metallic Oxides, Part A* (Elsevier Science Ltd., Amsterdam) (1980).
12. D. R. Lide, *CRC Handbook of Chemistry and Physics, Internet Version 2005* (CRC Press, Boca Raton, FL) (2005).
13. W. D. Ryden, A. W. Lawson, and C. C. Sartain, *Phys. Lett. A*, **26**, 209 (1968).
14. T. Hepel, *J. Electrochem. Soc.*, **132**, 2385 (1985).
15. S. Gottesfeld, J. D. E. McIntyre, G. Beni, and J. L. Shay, *Appl. Phys. Lett.*, **33**, 208 (1978).
16. L. D. Burke, J. K. Mulcahy, and D. P. Whelan, *J. Electroanal. Chem. Interfacial Electrochem.*, **163**, 117 (1984).
17. J. D. E. McIntyre, W. F. Peck, and S. Nakahara, *J. Electrochem. Soc.*, **127**, 1264 (1980).
18. A. A. F. Grupioni, E. Arashiro, and T. A. F. Lassali, *Electrochim. Acta*, **48**, 407 (2002).
19. J. Mozota and B. E. Conway, *Electrochim. Acta*, **28**, 1 (1983).
20. B. E. Conway and J. Mozota, *Electrochim. Acta*, **28**, 9 (1983).
21. M. Pourbaix, *Atlas of Electrochemical Equilibria in Aqueous Solutions* (National Association of Corrosion Engineers, Houston, TX) (1974).
22. J. D. E. McIntyre, S. Basu, W. F. Peck, W. L. Brown, and W. M. Augustyniak, *Phys. Rev. B*, **25**, 7242 (1982).
23. S. Gottesfeld and S. Srinivasan, *J. Electroanal. Chem.*, **86**, 89 (1978).
24. A. Minguzzi, O. Lugaresi, E. Achilli, C. Locatelli, A. Vertova, P. Ghigna, and S. Rondinini, *Chem. Sci.*, **5**, 3591 (2014).
25. E. Achilli, A. Minguzzi, O. Lugaresi, C. Locatelli, S. Rondinini, G. Spinolo, and P. Ghigna, *J. Spectrosc.*, **2014**, 1 (2014).
26. Y. Mo, I. C. Stefan, W. Cai, J. Dong, P. Carey, and D. A. Scherson, *J. Phys. Chem. B*, **106**, 3681 (2002).
27. M. Vuković, *J. Appl. Electrochem.*, **17**, 737 (1987).
28. M. Vuković, *J. Appl. Electrochem.*, **20**, 969 (1990).
29. T. Reier, D. Teschner, T. Lunkenbein, A. Bergmann, S. Selve, R. Kraehnert, R. Schlögl, and P. Strasser, *J. Electrochem. Soc.*, **161**, F876 (2014).
30. S. Cherevko, S. Geiger, O. Kasian, A. Mingers, and K. J. J. J. Mayrhofer, *J. Electroanal. Chem.*, **774**, 102 (2016).
31. S. Geiger, O. Kasian, B. R. Shrestha, A. M. Mingers, K. J. J. Mayrhofer, and S. Cherevko, *J. Electrochem. Soc.*, **163**, F3132 (2016).
32. E. J. Frazer and R. Woods, *J. Electroanal. Chem. Interfacial Electrochem.*, **102**, 127 (1979).
33. A. R. Hillman, M. A. Skopek, and S. J. Gurman, *Phys. Chem. Chem. Phys.*, **13**, 5252 (2011).
34. S. Cherevko, A. R. Zeradjanin, A. A. Topalov, N. Kulyk, I. Katsounaros, and K. J. J. Mayrhofer, *ChemCatChem*, **6**, 2219 (2014).
35. L. D. Burke and E. J. M. O'Sullivan, *J. Electroanal. Chem. Interfacial Electrochem.*, **117**, 155 (1981).
36. D. N. Buckley and L. D. Burke, *J. Chem. Soc. Faraday Trans. 1 Phys. Chem. Condens. Phases*, **71**, 1447 (1975).
37. D. F. Abbott, D. Lebedev, K. Waltar, M. Povia, M. Nachtegaal, E. Fabbri, C. Copéret, and T. J. Schmidt, *Chem. Mater.*, **28**, 6591 (2016).
38. N. Danilovic et al., *J. Phys. Chem. Lett.*, **5**, 2474 (2014).
39. S. H. Chang, J. G. Connell, N. Danilovic, R. Subbaraman, K.-C. Chang, V. R. Stamenkovic, and N. M. Markovic, *Faraday Discuss.*, **176**, 125 (2014).
40. S. Geiger et al., *Nat. Catal.*, **1**, 508 (2018).
41. Y. T. Kim et al., *Nat. Commun.*, **8**, 1449 (2017).
42. T. Binninger, R. Mohamed, K. Waltar, E. Fabbri, P. Levecque, R. Kötz, and T. J. Schmidt, *Sci. Rep.*, **5**, 12167 (2015).
43. R. S. Yeo, J. Orehotsky, W. Visscher, and S. Srinivasan, *J. Electrochem. Soc.*, **128**, 1900 (1981).
44. R. Kötz and S. Stucki, *J. Electrochem. Soc.*, **132**, 103 (1985).
45. R. Kötz and S. Stucki, *Electrochim. Acta*, **31**, 1311 (1986).
46. S. Cherevko, T. Reier, A. R. Zeradjanin, Z. Pawolek, P. Strasser, and K. J. J. J. Mayrhofer, *Electrochem. Commun.*, **48**, 81 (2014).
47. E. Rasten, G. Hagen, and R. Tunold, *ECS Proceedings: Energy Electrochem. Process a Clean. Environ.*, **2001–23**, 151 (2001).
48. E. Rasten, G. Hagen, and R. Tunold, *Electrochim. Acta*, **48**, 3945 (2003).
49. J. C. Cruz, V. Baglio, S. Siracusano, R. Ornelas, L. Ortiz-Frade, L. G. Arriaga, V. Antonucci, and a. S. Aricò, *J. Nanoparticle Res.*, **13**, 1639 (2011).
50. G. Li, H. Yu, X. Wang, S. Sun, Y. Li, Z. Shao, and B. Yi, *Phys. Chem. Chem. Phys.*, **15**, 2858 (2013).
51. T. Audichon, E. Mayousse, S. Morisset, C. Morais, C. Comminges, T. W. Napporn, and K. B. Kokoh, *Int. J. Hydrogen Energy*, **39**, 16785 (2014).
52. S. Zhao, A. Stocks, B. Rasimick, K. More, and H. Xu, *J. Electrochem. Soc.*, **165**, F82 (2018).
53. R. Hutchings, K. Müller, R. Kötz, and S. Stucki, *J. Mater. Sci.*, **19**, 3987 (1984).
54. E. Oakton, D. Lebedev, A. Fedorov, F. Krumeich, J. Tillier, O. Sereda, T. J. Schmidt, and C. Copéret, *New J. Chem.*, **40**, 1834 (2016).
55. V. I. Birss, H. Andreas, I. Serebrennikova, and H. Elzanowska, *Electrochem. Solid State Lett.*, **2**, 326 (1999).
56. F. Karimi, A. Bazylak, and B. A. Peppley, *J. Electrochem. Soc.*, **164**, F464 (2017).
57. G. C. da Silva, N. Perini, and E. A. Ticianelli, *Appl. Catal. B Environ.*, **218**, 287 (2017).
58. S. Ardizzone, A. Carugati, and S. Trasatti, *J. Electroanal. Chem.*, **126**, 287 (1981).
59. M. A. Petit and V. Plichon, *J. Electroanal. Chem.*, **444**, 247 (1998).
60. L. M. Schiavone, W. C. Dautremont-Smith, G. Beni, and J. L. Shay, *Appl. Phys. Lett.*, **35**, 823 (1979).
61. L. M. Schiavone, W. C. Dautremont-Smith, G. Beni, and J. L. Shay, *J. Electrochem. Soc.*, **128**, 1339 (1981).
62. W. Böld and M. Breiter, *Electrochim. Acta*, **5**, 169 (1961).
63. A. Capon and R. Parsons, *J. Electroanal. Chem. Interfacial Electrochem.*, **39**, 275 (1972).
64. D. A. J. Rand and R. Woods, *J. Electroanal. Chem. Interfacial Electrochem.*, **55**, 375 (1974).
65. J. M. Otten and W. Visscher, *J. Electroanal. Chem. Interfacial Electrochem.*, **55**, 1 (1974).
66. M. M. Lohrengel and J. W. Schultze, *Electrochim. Acta*, **21**, 957 (1976).
67. L. D. Burke and R. A. Scannell, *J. Electroanal. Chem. Interfacial Electrochem.*, **175**, 119 (1984).
68. P. G. Pickup and V. I. Birss, *J. Electroanal. Chem.*, **220**, 83 (1987).
69. S. Gottesfeld and J. D. E. McIntyre, *J. Electrochem. Soc.*, **126**, 742 (1979).
70. S. Cherevko, S. Geiger, O. Kasian, A. Mingers, and K. J. J. Mayrhofer, *J. Electroanal. Chem.*, **773**, 69 (2016).
71. D. Čukman and M. Vuković, *J. Electroanal. Chem. Interfacial Electrochem.*, **279**, 283 (1990).
72. Y. Sato, M. Yanagida, H. Yamanaka, and H. Tanigawa, *J. Electrochem. Soc.*, **136**, 863 (1989).
73. R. Sanjinés, A. Aruchamy, and F. Lévy, *J. Electrochem. Soc.*, **136**, 1740 (1989).
74. T. R. Ralph, S. Hudson, and D. P. Wilkinson, *ECS Trans.*, **1**, 67 (2006).
75. R. T. Atanasoski, L. L. Atanasoska, and D. A. Cullen, *Electrocatal. Fuel Cells A Non- Low- Platin. Approach*, ed. M. Shao (Springer, Berlin London) p. 637 (2013).
76. S. D. Knights, K. M. Colbow, J. St-Pierre, and D. P. Wilkinson, *J. Power Sources*, **127**, 127 (2004).
77. D. P. Wilkinson and J. St-Pierre, *Handb. Fuel Cells*, ed. W. Vielstich, A. Lamm, and H. A. Gasteiger (John Wiley & Sons, Ltd., Chichester, UK) p. 611 (2010).
78. J. Zhang, S. Kumaraguru, R. S. Kukreja, W. Gu, P. T. Yu, and B. Lakshmanan, *Proc. Int. Fuel Cell Work. 2015* (University of Yamanashi, Kofu, Japan) p. 23 (2015).
79. K. C. Neyerlin, W. Gu, J. Jorne, and H. A. Gasteiger, *J. Electrochem. Soc.*, **154**, B631 (2007).
80. J. Durst, C. Simon, F. Hasché, and H. A. Gasteiger, *J. Electrochem. Soc.*, **162**, F190 (2015).
81. J. Durst, A. Siebel, C. Simon, F. Hasché, J. Herranz, and H. A. Gasteiger, *Energy Environ. Sci.*, **7**, 2255 (2014).
82. H. S. C. O'Neill and J. Nell, *Geochim. Cosmochim. Acta*, **61**, 5279 (1997).
83. H. Beyer, S. Meini, N. Tsiouvaras, M. Piana, and H. A. Gasteiger, *Phys. Chem. Chem. Phys.*, **15**, 11025 (2013).
84. J. Zhang, H. A. Gasteiger, and W. Gu, *J. Electrochem. Soc.*, **160**, F616 (2013).
85. S. M. Alia, B. Rasimick, C. Ngo, K. C. Neyerlin, S. S. Kocha, S. Pylypenko, H. Xu, and B. S. Pivovar, *J. Electrochem. Soc.*, **163**, F3105 (2016).
86. M. Lopez, A. Schleunung, and P. Biberbach, *Precious Metal Oxide Catalyst For Water Electrolysis* (2009), EP 1 701 790 B1.
87. R. Blachnik, S. Koritnig, D. Steinmeier, A. Wilke, A. Feltz, and H. Reuter, *Taschenbuch Für Chemiker Und Physiker* (Springer, Berlin) 3 (1998).
88. W. Heiland et al., *Taschenbuch Für Chemiker Und Physiker* (Springer, Berlin, Heidelberg) 1 (1992).
89. K. Broka and P. Ekdunge, *J. Appl. Electrochem.*, **27**, 117 (1997).
90. C. K. Mittelsteadt and H. Liu, *Handb. Fuel Cells*, ed. W. Vielstich, A. Lamm, and H. A. Gasteiger (John Wiley & Sons, Ltd., Chichester, UK) p. 345 (2010).
91. B. Bensmann, R. Hanke-Rauschenbach, and K. Sundmacher, *Int. J. Hydrogen Energy*, **39**, 49 (2014).
92. B. Bensmann, R. Hanke-Rauschenbach, G. Müller-Syring, M. Henel, and K. Sundmacher, *Appl. Energy*, **167**, 107 (2016).
93. B. Bensmann, R. Hanke-Rauschenbach, I. K. Peña Arias, and K. Sundmacher, *Electrochim. Acta*, **110**, 570 (2013).
94. P. J. Rheinländer, M. Bernt, Y. Incedag, and H. A. Gasteiger, *Meet. Abstr.*, **MA2016-02**, 2427 (2016).
95. M. Schalenbach, M. Carmo, D. L. Fritz, J. Mergel, and D. Stolten, *Int. J. Hydrogen Energy*, **38**, 14921 (2013).
96. J. Durst et al., *ECS Trans.*, **69**, 67 (2015).
97. J. Juodkazytė, B. Šebeka, I. Valsiunas, and K. Juodkazis, *Electroanalysis*, **17**, 947 (2005).
98. A. Weiß, A. Siebel, M. Bernt, T.-H. Shen, V. Tileli, and H. A. Gasteiger, *J. Electrochem. Soc.*, **166**, F487 (2019).
99. E. Brightman, J. Dodwell, N. Van Dijk, and G. Hinds, *Electrochem. Commun.*, **52**, 1 (2015).

100. J. M. Otten and W. Visscher, *J. Electroanal. Chem. Interfacial Electrochem.*, **55**, 13 (1974).
101. G. Lodi, E. Sivieri, A. Debattisti, and S. Trasatti, *J. Appl. Electrochem.*, **8**, 135 (1978).
102. C. Rakousky, U. Reimer, K. Wippermann, S. Kuhri, M. Carmo, W. Lueke, and D. Stolten, *J. Power Sources*, **342**, 38 (2017).
103. S. A. Grigoriev, P. Millet, S. V. Korobtsev, V. I. Porembskiy, M. Pepic, C. Etievant, C. Puyenchet, and V. N. Fateev, *Int. J. Hydrogen Energy*, **34**, 5986 (2009).
104. R. Hanke-Rauschenbach, B. Bensmann, and P. Millet, *in Compend. Hydrog. Energy Hydrog. Prod. Purif.* (Elsevier Ltd.) p. 179 (2015).
105. B. L. Kienitz, H. Baskaran, and T. A. Zawodzinski, *Electrochim. Acta*, **54**, 1671 (2009).